Applied Mathematical Modelling 104 (2022) 67–95

Contents lists available at ScienceDirect

Applied Mathematical Modelling

journal homepage: www.elsevier.com/locate/apm

A three-dimensional model of wave interactions with permeable structures using the lattice Boltzmann method

Enbo Xing[a], Qinghe Zhang[a,*], Guangwei Liu[b], Jinfeng Zhang[a,c], Chaoqun Ji[a]

[a] State Key Laboratory of Hydraulic Engineering Simulation and Safety, Tianjin University, Tianjin 300072, China
[b] State Key Laboratory of Hydroscience and Engineering, Department of Hydraulic Engineering, Tsinghua University, Beijing 100084, China
[c] Key Laboratory of Earthquake Engineering Simulation and Seismic Resilience of China Earthquake Administration, Tianjin University, Tianjin 300350, China

ARTICLE INFO

Article history:
Received 22 April 2021
Revised 10 November 2021
Accepted 13 November 2021
Available online 22 November 2021

Keywords:
Lattice Boltzmann method
Volume-averaged Navier-Stokes equations
Porous media
Three-dimensional wave-structure interaction
Large eddy simulation
Volume-of-fluid method

ABSTRACT

To simulate the three-dimensional interaction of waves and porous structures using the lattice Boltzmann method, a novel multi-relaxation-time lattice Boltzmann scheme corresponding to the volume-averaged Navier-Stokes equations incorporating porous flow is developed. The porosity is introduced into the equilibrium distribution function, and the frictional forces produced by the porous media are added by the discrete force model. Through the Maxwell iteration, the relation between the mesoscopic lattice Boltzmann scheme and the macroscopic governing equations is established. Large eddy simulation and the single-phase volume-of-fluid techniques are modified to take porous media into account. The friction parameters in this model are calibrated using the experimental data of two-dimensional dam-break waves interacting with porous media composed of crushed rocks. Validations are carried out by comparing the simulation result of the proposed model with the laboratory data of three-dimensional dam-break waves impacting a prism and three-dimensional surface gravity waves (solitary waves and cnoidal waves) interacting with a vertical permeable breakwater. Furthermore, the interaction of regular waves and a rubble mound breakwater is used to test the capability of the model to handle spatially varying porous media. The different simulation results strongly agree with the experimental data, which prove that the lattice Boltzmann model has the ability to simulate complex wave motions near porous structures.

1. Introduction

Porous coastal structures such as breakwaters are widely used to protect coastal infrastructures or prevent natural shorelines from wave erosion. Knowledge of the interaction between waves and porous structures is of significance for understanding the mechanism of wave transformation and stability of structures.

With the development of computing power in recent years, numerical models have played increasingly significant roles in the investigation of the interactions between waves and porous structures. To date, two kinds of numerical models based on Navier-Stokes (N-S) equations have been widely used. One is a Eulerian grid-based model that solves the N-S equations by using the finite difference method (FDM) or finite volume method (FVM). Pioneering work was performed by Liu

* Corresponding author.
E-mail address: qhzhang@tju.edu.cn (Q. Zhang).

https://doi.org/10.1016/j.apm.2021.11.018
0307-904X/

et al. [1], who first derived the spatially averaged N-S equations assuming that the turbulence in porous media is negligible. To consider the turbulence both inside and outside a porous structure, Hsu et al. [2] developed a two-dimensional numerical model based on the volume-averaged Reynolds-averaged Navier-Stokes (VARANS) equations. Afterwards, a few 3D models were proposed to simulate wave-porous structure interactions. Hu et al. [3] studied dam-break wave interactions with porous structures using 3D volume-averaged Navier-Stokes (VANS) equations, where the turbulence was calculated by a large eddy simulation (LES); del Jesus et al. [4] re-derived the VARANS equations by means of a volume averaging process and calibrated the coefficient of porous resistance through dam-break cases. Then, Higuera et al. [5] developed a new model called IHFOAM that solves the VARANS equations using the open source software OpenFOAM.

Another numerical approach describing wave interaction with porous media is the Lagrangian meshfree model, in particular, the smooth particle hydrodynamics (SPH) model. Pioneering work was performed by Shao [6], who introduced the resistance force of porous media into the governing equations. Ren et al. [7] presented a weakly compressible SPH (WCSPH) model based on the spatially averaged N-S equations with sub-particle-scale turbulence closure only for external flow. Then, Ren et al. [8] calculated the porosity information at the fixed background points and determined the turbulence in both clear and porous regions. Khayyer et al. [9] proposed a numerical wave tank with variable porosity media based on incompressible SPH (ISPH). In recent years, the improved meshless local Petrov Galerkin method (IMLPG) has been successfully used in the 2D wave-porous interaction simulation with few nodes [10,11]. Regarding the Lagrangian meshfree method, 3D models for real applications are scarce because of the high computational demand. Wen et al. [12] developed a hybrid MPI-OpenMP SPH model to simulate 3D wave-structure interactions. However, to obtain the simulation results in an acceptable time, the wave flume was truncated and a short simulation period was adopted in their cases.

In general, due to the necessity of solving the pressure Poisson equation in the Eulerian grid-based model and ISPH model or using a large number of particles to achieve high-level results in the WCSPH model, several N-S type models have high computational costs and low parallel scalability, especially for 3D wave propagation applications. Recently, the lattice Boltzmann method (LBM) has emerged as a promising numerical wave approach due to its high parallel scalability and low computational costs [13–19]. However, the only work on the interaction of waves and porous structures using the LBM has been a 2D model presented by Badarch et al. [15], who used the relationship between the porosity and permeability established by Walsh et al. [20]. The partial-bounceback scheme they used could not recover the macroscopic VANS equations and the porosity in their model became an adjustable parameter rather than a constant reflecting the material properties. Furthermore, due to the lack of a nonlinear resistance force term, their model may show deviation in the large porosity case, for which the flow is usually in the turbulent regime [21]. To the knowledge of the authors, there are currently no validated LBM models with complete theoretical derivation for wave-porous structure interactions, although two different approaches that try to simulate the porous flow through a porous medium in the LBM have been presented. The first approach describes porous media at the pore scale and is thus suitable for studying the microscopic interaction between the fluid and solid skeleton [22–27]. However, the size of the simulation domain may be limited because that it needs a large amount of lattice nodes to describe the pores of porous media [28]. To simulate porous media at the engineering scale, another approach uses macroscopic information to eliminate the need to describe the pores of porous media. For example, the early work of Guo and Zhao [28] modified the lattice Boltzmann (LB) scheme by adding an additional force term to represent the resistance of porous media, but can be used only for cases of uniform porosity because the pressure term of the VANS equations cannot be totally recovered through the Chapman-Enskog expansion. Zhang et al. [29] tried to introduce a pressure correction term to fix the above problem, but their method caused numerical instability according to the analysis of Blais et al. [30]. Blais et al. [30] introduced multiple non-physical correction terms with loose locality, which affected the parallel scalability of the LBM. Höcker et al. [31] proposed a modification of the streaming step in the LBM scheme to retrieve the pressure term in the momentum equation of VANS. Nonetheless, the continuity equation cannot be recovered due to this modification. Moreover, all the above models are designed in two-dimensional without incorporating the free surface motion, which means that these methods are unable to simulate 3D wave-porous structure interactions.

Therefore, the objective of the present paper is first to derive a stable 3D VANS-LB scheme that can recover the VANS equations through Maxwell iteration. Additionally, the LES is used to take into account the effect of turbulence both inside and outside of porous medium. Through the addition of the newly proposed VANS-LB scheme to the 3D numerical wave tanks developed by Liu et al. [19], the interactions of waves with homogeneous and heterogeneous porous structures can be simulated at the macroscopic scale.

This paper is organized as follows. After the introduction, the macroscopic governing equations and the novel VANS-LB scheme are presented in Section 2. A calibration of the porous medium resistance coefficients of the new VANS-LB scheme using porous dam-break cases is presented in Section 3. Validations of the 3D LBM model of wave-porous structure interactions are presented in Section 4. The computational efficiency without MPI is discussed in Section 5. The concluding remarks are presented in Section 6.

2. Numerical model

The macroscopic governing equations of the porous medium flow are the VANS equations, which are achieved by the volume averaging of the incompressible N-S equations. With the use of a suitable kernel function, the filtering process of the LES is identical to the volume averaging process [3]. The volume averaging process eliminates the need for complex geometry information from the porous medium and replaces this information by the resistance force with empirical friction

parameters related to the macroscopic material properties. The VANS equations are discretized by the LBM using the newly proposed VANS-LB scheme in this section.

2.1. Macroscopic governing equations

In this paper, the same volume averaging process as that used by del Jesus et al. [4] is applied directly on the incompressible N-S equations, which is widely used and can address heterogeneous porous media. The macroscopic governing equations are given as:

$$\frac{\partial}{\partial x_i}\frac{\langle u_i\rangle}{\phi} = 0 \tag{1}$$

$$\frac{\partial}{\partial t}\frac{\langle u_i\rangle}{\phi} + \frac{\langle u_j\rangle}{\phi}\frac{\partial}{\partial x_j}\frac{\langle u_i\rangle}{\phi} = -\frac{1}{\rho}\frac{\partial}{\partial x_i}p + g_i + \frac{\partial}{\partial x_i}\left(\nu_{total}\frac{\partial}{\partial x_j}\frac{\langle u_i\rangle}{\phi}\right) - [CT]_p \tag{2}$$

where $\langle u\rangle$ is the averaged velocity (also called the Darcy velocity); p is the pressure; ρ is the density; g is the acceleration of gravity; ϕ is the porosity, which is defined as $\phi = V_f/V$; V is the averaging volume; and V_f is the fluid phase occupied volume in the averaging volume. The relation between the intrinsic magnitude and averaged magnitude can be expressed as $\langle a\rangle = \phi\langle a\rangle^f$. ν_{total} is the total viscosity and is defined as $\nu_{total} = \nu + \nu_t$, where ν is the kinematic viscosity and ν_t is the eddy viscosity related to turbulence flow. ν_t can be calculated by $\nu_t = (C_s\Delta)^2\sqrt{2\langle S_{ij}\rangle^f\langle S_{ij}\rangle^f}$, where C_s is the Smagorinsky coefficient, which can be set as a constant between 0.05-0.18. Δ is the filter length, which can be calculated as a function of the grid width in all three directions $\Delta = (\phi\delta x\delta y\delta z)^{1/3}$ when the filtering kernel is the grid filter. Note that the filter length takes into account only the volume occupied by fluid [32]. S_{ij} is the strain rate tensor, which is given as $S_{ij} = (\partial u_i/\partial x_j + \partial u_j/\partial x_i)/2$.

The last term in Eq. (2) represents the porous medium closure terms. To maintain the quadratic nature when calculating the macroscopic velocity in the LBM, we choose the porous medium closure term without a transitional parameter, which can be expressed as:

$$[CT]_p = a\frac{\langle u_i\rangle}{\phi} + b\frac{\langle u_i\rangle}{\phi}\left|\frac{\langle u_i\rangle}{\phi}\right| + c\frac{\partial}{\partial t}\frac{\langle u_i\rangle}{\phi} \tag{3}$$

where the first term on the right-hand side is the linear (Darcy) term, which dominates in laminar flow; the second term is the nonlinear (Forcheimer) term, which dominates in turbulent flow; and the third term takes into account the unsteady flow, as proposed by Polubarinova-Kochina [33]. *a, b, c* are three constants that need to be calculated by empirical formulas. Engelund's formulas [34] modified by van Gent [35] can be used to determine the constants. The formulas are presented as follows:

$$a = \alpha\frac{(1-\phi)^3}{\phi^2}\frac{\nu}{D_{50}^2} \tag{4}$$

$$b = \beta\left(1 + \frac{7.5}{KC}\right)\frac{1-\phi}{\phi^2 D_{50}} \tag{5}$$

$$c = \gamma\frac{1-\phi}{\phi} \tag{6}$$

where D_{50} is the mean nominal diameter and *KC* is the Keulegan-Carpenter number, which takes into account the resistance force produced by the oscillation of the unsteady flow (such as waves). The number is calculated by $KC = T_0 u_m/D_{50}\phi$, where u_m is the maximum oscillation velocity and T_0 is the characteristic period. α, β are friction parameters that need further calibration. γ has been proven to have less influence in most cases and is suggested to equal 0.34 by del Jesus et al. [4].

2.2. LBM for VANS equations

2.2.1. A modified VANS-LB scheme

The LBM can be considered as a technique for discretizing the N-S type equations. The equations are discretized in the discrete velocity ($\mathbf{e}_\alpha$) space. The multi-relaxation-time (MRT) lattice Boltzmann equation (LBE) with a force term is given as [36]:

$$f_\alpha(\mathbf{x} + \mathbf{e}_\alpha\delta t, t + \delta t) - f_\alpha(\mathbf{x}, t) = -\mathbf{M}^{-1}\left[\hat{\mathbf{S}}(\mathbf{m} - \mathbf{m}^{eq})\right] + \mathbf{M}^{-1}\mathbf{\Phi}\delta t \tag{7}$$

where $f_\alpha(\mathbf{x},t)$ is the fluid particle velocity distribution function at position $\mathbf{x}$ and time t; δt is the time step; and δx is the lattice length. For the D3Q27 model, the discrete velocities ($\mathbf{e}_\alpha$) are three-dimensional and contain 27 subcomponents and can be expressed as:

$$\mathbf{e}_\alpha = c\begin{bmatrix} 0 & 1 & -1 & 0 & 0 & 0 & 0 & 1 & -1 & 1 & -1 & 1 & -1 & 1 & -1 & 0 & 0 & 0 & 0 & 1 & -1 & 1 & -1 & 1 & -1 & -1 & 1 \\ 0 & 0 & 0 & 1 & -1 & 0 & 0 & 1 & 1 & -1 & -1 & 0 & 0 & 0 & 0 & 1 & -1 & 1 & -1 & 1 & -1 & 1 & -1 & -1 & 1 & 1 & -1 \\ 0 & 0 & 0 & 0 & 0 & 1 & -1 & 0 & 0 & 0 & 0 & 1 & 1 & -1 & -1 & 1 & 1 & -1 & -1 & 1 & -1 & -1 & 1 & 1 & -1 & 1 & -1 \end{bmatrix}^T \tag{8}$$

where $c = \delta x/\delta t$. $\mathbf{M}$ and $\mathbf{M}^{-1}$ are the transformation matrix and inverse transformation matrix, respectively, where the transformation matrix in the D3Q27 model is given by [19]:

$$\mathbf{M} = \begin{bmatrix}
1 & 1 & 1 & 1 & 1 & 1 & 1 & 1 & 1 & 1 & 1 & 1 & 1 & 1 & 1 & 1 & 1 & 1 & 1 & 1 & 1 & 1 & 1 & 1 & 1 & 1 & 1 \\
0 & 1 & -1 & 0 & 0 & 0 & 0 & 1 & -1 & 1 & -1 & 1 & -1 & 1 & -1 & 0 & 0 & 0 & 0 & 1 & -1 & 1 & -1 & 1 & -1 & -1 & 1 \\
0 & 0 & 0 & 1 & -1 & 0 & 0 & 1 & 1 & -1 & -1 & 0 & 0 & 0 & 0 & 1 & -1 & 1 & -1 & 1 & -1 & 1 & -1 & -1 & 1 & 1 & -1 \\
0 & 0 & 0 & 0 & 0 & 1 & -1 & 0 & 0 & 0 & 0 & 1 & 1 & -1 & -1 & 1 & 1 & -1 & -1 & 1 & -1 & -1 & 1 & 1 & -1 & 1 & -1 \\
-1 & 0 & 0 & 0 & 0 & 0 & 0 & 1 & 1 & 1 & 1 & 1 & 1 & 1 & 1 & 1 & 1 & 1 & 1 & 2 & 2 & 2 & 2 & 2 & 2 & 2 & 2 \\
0 & 2 & 2 & -1 & -1 & -1 & -1 & 1 & 1 & 1 & 1 & 1 & 1 & 1 & 1 & -2 & -2 & -2 & -2 & 0 & 0 & 0 & 0 & 0 & 0 & 0 & 0 \\
0 & 0 & 0 & 1 & 1 & -1 & -1 & 1 & 1 & 1 & 1 & -1 & -1 & -1 & -1 & 0 & 0 & 0 & 0 & 0 & 0 & 0 & 0 & 0 & 0 & 0 & 0 \\
0 & 0 & 0 & 0 & 0 & 0 & 0 & 1 & -1 & -1 & 1 & 0 & 0 & 0 & 0 & 0 & 0 & 0 & 0 & 1 & 1 & 1 & 1 & -1 & -1 & -1 & -1 \\
0 & 0 & 0 & 0 & 0 & 0 & 0 & 0 & 0 & 0 & 0 & 0 & 0 & 0 & 0 & 1 & -1 & -1 & 1 & 1 & 1 & -1 & -1 & -1 & -1 & 1 & 1 \\
0 & 0 & 0 & 0 & 0 & 0 & 0 & 0 & 0 & 0 & 0 & 1 & -1 & -1 & 1 & 0 & 0 & 0 & 0 & 1 & 1 & -1 & -1 & 1 & 1 & -1 & -1 \\
0 & -2 & 2 & 0 & 0 & 0 & 0 & 1 & -1 & 1 & -1 & 1 & -1 & 1 & -1 & 0 & 0 & 0 & 0 & 4 & -4 & 4 & -4 & 4 & -4 & -4 & 4 \\
0 & 0 & 0 & -2 & 2 & 0 & 0 & 1 & 1 & -1 & -1 & 0 & 0 & 0 & 0 & 1 & -1 & 1 & -1 & 4 & -4 & 4 & -4 & -4 & 4 & 4 & -4 \\
0 & 0 & 0 & 0 & 0 & -2 & 2 & 0 & 0 & 0 & 0 & 1 & 1 & -1 & -1 & 1 & 1 & -1 & -1 & 4 & -4 & -4 & 4 & 4 & -4 & 4 & -4 \\
0 & 1 & -1 & 0 & 0 & 0 & 0 & -1 & 1 & -1 & 1 & -1 & 1 & -1 & 1 & 0 & 0 & 0 & 0 & 0 & 0 & 0 & 0 & 0 & 0 & 0 & 0 \\
0 & 0 & 0 & 1 & -1 & 0 & 0 & -1 & -1 & 1 & 1 & 0 & 0 & 0 & 0 & -1 & 1 & -1 & 1 & 0 & 0 & 0 & 0 & 0 & 0 & 0 & 0 \\
0 & 0 & 0 & 0 & 0 & 1 & -1 & 0 & 0 & 0 & 0 & -1 & -1 & 1 & 1 & -1 & -1 & 1 & 1 & 0 & 0 & 0 & 0 & 0 & 0 & 0 & 0 \\
1 & -1 & -1 & -1 & -1 & -1 & -1 & 0 & 0 & 0 & 0 & 0 & 0 & 0 & 0 & 0 & 0 & 0 & 0 & 4 & 4 & 4 & 4 & 4 & 4 & 4 & 4 \\
-3 & 4 & 4 & 4 & 4 & 4 & 4 & -4 & -4 & -4 & -4 & -4 & -4 & -4 & -4 & -4 & -4 & -4 & -4 & 0 & 0 & 0 & 0 & 0 & 0 & 0 & 0 \\
0 & -2 & -2 & 1 & 1 & 1 & 1 & 2 & 2 & 2 & 2 & 2 & 2 & 2 & 2 & -4 & -4 & -4 & -4 & 0 & 0 & 0 & 0 & 0 & 0 & 0 & 0 \\
0 & 0 & 0 & -1 & -1 & 1 & 1 & 2 & 2 & 2 & 2 & -2 & -2 & -2 & -2 & 0 & 0 & 0 & 0 & 0 & 0 & 0 & 0 & 0 & 0 & 0 & 0 \\
0 & 0 & 0 & 0 & 0 & 0 & 0 & -1 & 1 & 1 & -1 & 0 & 0 & 0 & 0 & 0 & 0 & 0 & 0 & 2 & 2 & 2 & 2 & -2 & -2 & -2 & -2 \\
0 & 0 & 0 & 0 & 0 & 0 & 0 & 0 & 0 & 0 & 0 & 0 & 0 & 0 & 0 & -1 & 1 & 1 & -1 & 2 & 2 & -2 & -2 & -2 & -2 & 2 & 2 \\
0 & 0 & 0 & 0 & 0 & 0 & 0 & 0 & 0 & 0 & 0 & -1 & 1 & 1 & -1 & 0 & 0 & 0 & 0 & 2 & 2 & -2 & -2 & 2 & 2 & -2 & -2 \\
0 & 0 & 0 & 0 & 0 & 0 & 0 & 1 & -1 & 1 & -1 & -1 & 1 & -1 & 1 & 0 & 0 & 0 & 0 & 0 & 0 & 0 & 0 & 0 & 0 & 0 & 0 \\
0 & 0 & 0 & 0 & 0 & 0 & 0 & -1 & -1 & 1 & 1 & 0 & 0 & 0 & 0 & 1 & -1 & 1 & -1 & 0 & 0 & 0 & 0 & 0 & 0 & 0 & 0 \\
0 & 0 & 0 & 0 & 0 & 0 & 0 & 0 & 0 & 0 & 0 & 1 & 1 & -1 & -1 & -1 & -1 & 1 & 1 & 0 & 0 & 0 & 0 & 0 & 0 & 0 & 0 \\
0 & 0 & 0 & 0 & 0 & 0 & 0 & 0 & 0 & 0 & 0 & 0 & 0 & 0 & 0 & 0 & 0 & 0 & 0 & 1 & -1 & -1 & 1 & -1 & 1 & -1 & 1
\end{bmatrix} \tag{9}$$

$\hat{\mathbf{S}}$ is the relaxation parameter matrix, which can be modified to improve the stability of the model and is defined as:

$$\hat{\mathbf{S}} \equiv diag(1, 1, 1, 1, s_e, s_p, s_p, s_\nu, s_\nu, s_\nu, s_q, s_q, s_q, s_{q\varepsilon}, s_{q\varepsilon}, s_{q\varepsilon}, s_\varepsilon, s_{e3}, s_{\pi xx}, s_{\pi xx}, s_\pi, s_\pi, s_\pi, s_m, s_m, s_m) \tag{10}$$

where $s_e = 0.3$ and $s_p = s_\nu = \frac{1}{\tau_{total}}.\tau_{total}$ is calculated from the LES in the LBM. s_q,$s_{q\varepsilon}$,s_ε,s_{e3},$s_{\pi xx}$,s_π,s_m are relaxation parameters related to moments higher than the third order and do not influence the results. $\mathbf{m} = \mathbf{M} \bullet \mathbf{f}$ is the moment vector of the distribution function, where $\mathbf{f} \equiv [f_0, f_1, \ldots, f_{26}]$ is the vector of the distribution function. $\mathbf{m}^{eq} = \mathbf{M} \bullet \mathbf{f}^{eq}$ is the moment vector of the equilibrium distribution function, where $\mathbf{f}^{eq} \equiv [f_0^{eq}, f_1^{eq}, \ldots, f_{26}^{eq}]$ is the vector of the equilibrium distribution function. $\mathbf{\Phi} = \mathbf{MG}$ is the expression of the discrete force in the moment space, where $\mathbf{G} \equiv [G_0, G_1, \ldots, G_{26}]$ is the vector of the discrete force.

Different from the original LB scheme, the new LB scheme needs to recover the VANS equations of Eqs. (1) and (2). Hence, the scheme should contain the porosity and resistance force due to porous media. The adapted equilibrium distribution function is given by:

$$f_\alpha^{eq} = \frac{\omega_\alpha}{c_s^2}\left[\langle p \rangle^f + \frac{\mathbf{e}_\alpha \cdot \langle \mathbf{u} \rangle}{\phi} + \frac{(\mathbf{e}_\alpha \cdot \langle \mathbf{u} \rangle)^2}{2\phi^2 c_s^2} - \frac{\langle \mathbf{u} \rangle \cdot \langle \mathbf{u} \rangle}{2\phi^2}\right] \tag{11}$$

where p is the modified pressure proposed by Liu et al. [17]; $\langle \mathbf{u} \rangle = (\langle u_x \rangle, \langle u_y \rangle, \langle u_z \rangle)$ is the averaged velocity containing three direction components; c_s is the sound speed and the relation between c_s and c is $c_s^2 = c^2/3$; and ω_α are the weight coefficients of each discrete velocity component and is given by:

$$\omega_\alpha = \begin{cases} \frac{8}{27}, \alpha = 0 \\ \frac{2}{27}, \alpha = 1 \sim 6 \\ \frac{1}{54}, \alpha = 7 \sim 18 \\ \frac{1}{216}, \alpha = 19 \sim 26 \end{cases} \tag{12}$$

Therefore, $\mathbf{m}^{eq}$ is calculated as follows:

$$\mathbf{m}^{eq} = [3p, \frac{\langle u_x\rangle}{\phi}, \frac{\langle u_y\rangle}{\phi}, \frac{\langle u_z\rangle}{\phi}, \frac{\langle u_x\rangle^2 + \langle u_y\rangle^2 + \langle u_z\rangle^2}{\phi^2}, \frac{2\langle u_x\rangle^2 - \langle u_y\rangle^2 - \langle u_z\rangle^2}{\phi^2}, \frac{\langle u_y\rangle^2 - \langle u_z\rangle^2}{\phi^2}, \frac{\langle u_x\rangle\langle u_y\rangle}{\phi^2}, \frac{\langle u_y\rangle\langle u_z\rangle}{\phi^2}, \frac{\langle u_x\rangle\langle u_z\rangle}{\phi^2}, 0, 0, \ldots, 0]^T \tag{13}$$

The discrete force term G_α based on the Guo-Zheng-Shi force model [37] is also modified as:

$$G_a = \omega_a\left(\mathbf{I} - \frac{\hat{\mathbf{S}}}{2}\right)\left[\frac{\mathbf{e}_\alpha \cdot \mathbf{F}}{c_s^2} + \frac{\langle\mathbf{u}\rangle\mathbf{F} : \left(\mathbf{e}_\alpha\mathbf{e}_a - c_s^2\mathbf{I}\right)}{\phi c_s^4}\right] \tag{14}$$

where $\mathbf{F} = (F_x,F_y,F_z)$ represents the resistance force induced by the porous medium in different directions and can be related to the closure term in Eq. (2) by $\mathbf{F} = -[CT]_p$. Therefore, Φ is calculated as follows:

$$\mathbf{\Phi} = [0, h_1F_x, h_2F_y, h_3F_z, 2h_4\frac{\langle u_x\rangle F_x + \langle u_y\rangle F_y + \langle u_z\rangle F_z}{\phi}, 2h_5\frac{2\langle u_x\rangle F_x - \langle u_y\rangle F_y - \langle u_z\rangle F_z}{\phi}, 2h_6\frac{\langle u_y\rangle F_y - \langle u_z\rangle F_z}{\phi}, h_7\frac{\langle u_x\rangle F_y + \langle u_y\rangle F_x}{\phi}, h_8\frac{\langle u_y\rangle F_z + \langle u_z\rangle F_y}{\phi}, h_9\frac{\langle u_x\rangle F_z + \langle u_z\rangle F_x}{\phi}, 0, 0, \ldots, 0]^T \tag{15}$$

where h_α represent the parameters to be determined through subsequent analysis.

The macroscopic quantities can be recovered by taking the moments of the distribution functions, as given by:

$$\rho = \sum_\alpha f_\alpha \tag{16}$$

$$\frac{\rho_0\langle\mathbf{u}\rangle}{\phi} = \sum_\alpha f_\alpha\mathbf{e}_\alpha + \frac{1}{2}\delta_t\mathbf{F} \tag{17}$$

Unlike the original LB scheme, the macroscopic velocity cannot be calculated directly from the distribution function due to the appearance of the force term. In addition, the force term **F** caused by the porous medium is related to the macroscopic velocity. Therefore, Eq. (17) is rewritten as:

$$\frac{\rho_0\langle\mathbf{u}\rangle^n}{\phi} = \sum_\alpha f_\alpha\mathbf{e}_\alpha - \frac{1}{2}\delta_t\left(a\frac{\langle\mathbf{u}\rangle^n}{\phi} + b\frac{\langle\mathbf{u}\rangle^n}{\phi}\left|\frac{\langle\mathbf{u}\rangle^n}{\phi}\right|\right) - \frac{1}{2}c\left(\frac{\langle\mathbf{u}\rangle^n}{\phi} - \frac{\langle\mathbf{u}\rangle^{n-1}}{\phi}\right) \tag{18}$$

where the superscripts represent the time step of the quantity. Due to the quadratic nature of Eq. (18), the macroscopic velocity can be explicitly solved according to Guo and Zhao [28]:

$$\frac{\langle\mathbf{u}\rangle^n}{\phi} = \frac{\mathbf{v}}{c_0 + \sqrt{c_0^2 + c_1|\mathbf{v}|}} \tag{19}$$

where **v** is the middle velocity, defined as:

$$\mathbf{v} = \sum_\alpha f_\alpha\mathbf{e}_\alpha + c\frac{\langle\mathbf{u}\rangle^{n-1}}{2\phi} \tag{20}$$

c_0,c_1 are two parameters given by:

$$c_0 = \frac{1}{2}\left[1 + \frac{\delta t}{2}(a + c)\right] \tag{21}$$

$$c_1 = \frac{\delta t}{2}b \tag{22}$$

The turbulence both inside and outside the porous medium is calculated by the Smagorinsky eddy viscosity model proposed by Krafczyk et al. [38]. The specific implementation in our model has been thoroughly described by Liu et al. [19].

2.2.2. Derivation of macroscopic equations

The Maxwell iteration proposed by Yong et al. [39] is carried out to derive the macroscopic equations corresponding to the modified VANS-LB scheme. The first-order and second-order iteration results are given as:

$$\mathbf{m} = \left[\mathbf{I} - \delta t\widehat{\mathbf{S}}^{-1}\cdot\widetilde{\mathbf{D}}\right]\cdot\mathbf{m}^{eq} + \delta t\widehat{\mathbf{S}}^{-1}\cdot\mathbf{\Phi} + O\left(\delta t^2\right) \tag{23}$$

$$\mathbf{m} = \mathbf{m}^{eq} - \delta t\hat{\mathbf{S}}^{-1}\cdot\widetilde{\mathbf{D}}\cdot\left[\mathbf{I} - \delta t\left(\hat{\mathbf{S}}^{-1} - \frac{\mathbf{I}}{2}\right)\cdot\widetilde{\mathbf{D}}\right]\cdot\mathbf{m}^{eq} + \delta t\left(\mathbf{I} - \delta t\hat{\mathbf{S}}^{-1}\cdot\widetilde{\mathbf{D}}\right)\hat{\mathbf{S}}^{-1}\cdot\mathbf{\Phi} + O\left(\delta t^3\right) \tag{24}$$

where $\tilde{\mathbf{D}} = \mathbf{M}\cdot\mathbf{D}\cdot\mathbf{M}$, and $\mathbf{D}$ is the diagonal matrix-valued operator with the diagonal elements $\partial_t + \mathbf{e}_\alpha \bullet \nabla$.

With the substitution of Eqs. (13) and (15) into the first-order iteration result and applying the accurate expressions of the density (m_0) and momenta (m_1,m_2,m_3), the Euler equations can be obtained as:

$$\frac{\partial}{\partial x_i}\frac{\langle u_i\rangle}{\phi} = O(\delta t) \tag{25}$$

$$\frac{\partial}{\partial t}\frac{\langle u_i\rangle}{\phi} + \frac{\partial}{\partial x_i}\left(\frac{1}{\phi^2}\langle u_i\rangle\langle u_j\rangle\right) = -\frac{1}{\rho_0}\frac{\partial}{\partial x_i}p + \left(\frac{1}{2}+h_i\right)F_i + O(\delta t) \tag{26}$$

Therefore, $h_1 = h_2 = h_3 = 1/2$. Using Eqs. (25) and (26), the first ten matrix elements in $\tilde{\mathbf{D}}\cdot\mathbf{m}^{eq}$ can be simplified as:

$$\tilde{\mathbf{D}}\cdot\mathbf{m}^{eq} = \begin{pmatrix} O(\delta_t) \\ F_x + O(\delta_t) \\ F_y + O(\delta_t) \\ F_z + O(\delta_t) \\ \frac{1}{\phi}\langle\mathbf{u}\rangle\cdot\mathbf{F} + O(\delta_t) + O\left(u^3\right) \\ -\frac{2}{3}\left(-2\frac{\partial}{\partial x}\frac{\langle u_x\rangle}{\phi} + \frac{\partial}{\partial y}\frac{\langle u_y\rangle}{\phi} + \frac{\partial}{\partial z}\frac{\langle u_z\rangle}{\phi}\right) + \frac{2}{\phi}(2\langle u_x\rangle F_x - \langle u_y\rangle F_y - \langle u_z\rangle F_z) + O(\delta_t) + O\left(u^3\right) \\ \frac{2}{3}\left(-\frac{\partial}{\partial z}\frac{\langle u_z\rangle}{\phi} + \frac{\partial}{\partial y}\frac{\langle u_y\rangle}{\phi}\right) + \frac{2}{\phi}(\langle u_y\rangle F_y - \langle u_z\rangle F_z) + O(\delta_t) + O\left(u^3\right) \\ \frac{1}{3}\left(\frac{\partial}{\partial y}\frac{\langle u_x\rangle}{\phi} + \frac{\partial}{\partial x}\frac{\langle u_y\rangle}{\phi}\right) + \frac{1}{\phi}(\langle u_y\rangle F_x + \langle u_x\rangle F_y) + O(\delta_t) + O\left(u^3\right) \\ \frac{1}{3}\left(\frac{\partial}{\partial y}\frac{\langle u_z\rangle}{\phi} + \frac{\partial}{\partial z}\frac{\langle u_y\rangle}{\phi}\right) + \frac{1}{\phi}(\langle u_y\rangle F_z + \langle u_z\rangle F_y) + O(\delta_t) + O\left(u^3\right) \\ \frac{1}{3}\left(\frac{\partial}{\partial x}\frac{\langle u_z\rangle}{\phi} + \frac{\partial}{\partial z}\frac{\langle u_x\rangle}{\phi}\right) + \frac{1}{\phi}(\langle u_x\rangle F_z + \langle u_z\rangle F_x) + O(\delta_t) + O\left(u^3\right) \\ \cdots \end{pmatrix} \tag{27}$$

To derive the NS equations, the density and velocity related to the second-order iteration result can be written as:

$$\left(\tilde{\mathbf{D}}\cdot\mathbf{m}^{eq}\right)_0 = \mathbf{\Phi}_0 + \delta_t\left\{\begin{array}{l} \frac{\partial}{\partial t}\left[\tilde{\tau}_0\left(\tilde{\mathbf{D}}\cdot\mathbf{m}^{eq}\right)_0 - \tau_0\mathbf{\Phi}_0\right] \\ +\frac{\partial}{\partial x}\left[\tilde{\tau}_1\left(\tilde{\mathbf{D}}\cdot\mathbf{m}^{eq}\right)_1 - \tau_1\mathbf{\Phi}_1\right] \\ +\frac{\partial}{\partial y}\left[\tilde{\tau}_2\left(\tilde{\mathbf{D}}\cdot\mathbf{m}^{eq}\right)_2 - \tau_2\mathbf{\Phi}_2\right] \\ +\frac{\partial}{\partial z}\left[\tilde{\tau}_3\left(\tilde{\mathbf{D}}\cdot\mathbf{m}^{eq}\right)_3 - \tau_3\mathbf{\Phi}_3\right] \end{array}\right\} + O\left(\delta_t^2\right) \tag{28}$$

$$\left(\tilde{\mathbf{D}}\cdot\mathbf{m}^{eq}\right)_1 = \mathbf{\Phi}_1 + \delta_t\left\{\begin{array}{l} \frac{\partial}{\partial t}\left[\tilde{\tau}_1\left(\tilde{\mathbf{D}}\cdot\mathbf{m}^{eq}\right)_1 - \tau_1\mathbf{\Phi}_1\right] \\ +\frac{\partial}{\partial x}\left[\begin{array}{l} \frac{1}{3}\tilde{\tau}_0\left(\tilde{\mathbf{D}}\cdot\mathbf{m}^{eq}\right)_0 + \frac{1}{3}\tilde{\tau}_4\left(\tilde{\mathbf{D}}\cdot\mathbf{m}^{eq}\right)_4 \\ +\frac{1}{3}\tilde{\tau}_5\left(\tilde{\mathbf{D}}\cdot\mathbf{m}^{eq}\right)_5 \\ -\frac{1}{3}\tau_0\mathbf{\Phi}_0 - \frac{1}{3}\tau_4\mathbf{\Phi}_4 - \frac{1}{3}\tau_5\mathbf{\Phi}_5 \end{array}\right] \\ +\frac{\partial}{\partial y}\left[\tilde{\tau}_7\left(\tilde{\mathbf{D}}\cdot\mathbf{m}^{eq}\right)_7 - \tau_7\mathbf{\Phi}_7\right] \\ +\frac{\partial}{\partial z}\left[\tilde{\tau}_9\left(\tilde{\mathbf{D}}\cdot\mathbf{m}^{eq}\right)_9 - \tau_9\mathbf{\Phi}_9\right] \end{array}\right\} + \frac{1}{2}F_x + O\left(\delta t^2\right) \tag{29}$$

$$\left(\tilde{\mathbf{D}}\cdot\mathbf{m}^{eq}\right)_2=\mathbf{\Phi}_2+\delta_t\left\{\begin{array}{l}\frac{\partial}{\partial t}\left[\tilde{\tau}_2\left(\tilde{\mathbf{D}}\cdot\mathbf{m}^{eq}\right)_2-\tau_2\mathbf{\Phi}_2\right]\\+\frac{\partial}{\partial y}\left[\begin{array}{l}\frac{1}{3}\tilde{\tau}_0\left(\tilde{\mathbf{D}}\cdot\mathbf{m}^{eq}\right)_0+\frac{1}{3}\tilde{\tau}_4\left(\tilde{\mathbf{D}}\cdot\mathbf{m}^{eq}\right)_4\\-\frac{1}{6}\tilde{\tau}_5\left(\tilde{\mathbf{D}}\cdot\mathbf{m}^{eq}\right)_5+\frac{1}{3}\tilde{\tau}_6\left(\tilde{\mathbf{D}}\cdot\mathbf{m}^{eq}\right)_6\\-\frac{1}{3}\tau_0\mathbf{\Phi}_0-\frac{1}{3}\tau_4\mathbf{\Phi}_4+\frac{1}{6}\tau_5\mathbf{\Phi}_5-\frac{1}{2}\tau_6\mathbf{\Phi}_6\end{array}\right]\\+\frac{\partial}{\partial x}\left[\tilde{\tau}_7\left(\tilde{\mathbf{D}}\cdot\mathbf{m}^{eq}\right)_7-\tau_7\mathbf{\Phi}_7\right]\\+\frac{\partial}{\partial z}\left[\tilde{\tau}_8\left(\tilde{\mathbf{D}}\cdot\mathbf{m}^{eq}\right)_8-\tau_8\mathbf{\Phi}_8\right]\end{array}\right\}+\frac{1}{2}F_y+O\left(\delta t^2\right)\tag{30}$$

$$\left(\tilde{\mathbf{D}}\cdot\mathbf{m}^{eq}\right)_3=\mathbf{\Phi}_3+\delta_t\left\{\begin{array}{l}\frac{\partial}{\partial t}\left[\tilde{\tau}_3\left(\tilde{\mathbf{D}}\cdot\mathbf{m}^{eq}\right)_3-\tau_3\mathbf{\Phi}_3\right]\\+\frac{\partial}{\partial z}\left[\begin{array}{l}\frac{1}{3}\tilde{\tau}_0\left(\tilde{\mathbf{D}}\cdot\mathbf{m}^{eq}\right)_0+\frac{1}{3}\tilde{\tau}_4\left(\tilde{\mathbf{D}}\cdot\mathbf{m}^{eq}\right)_4-\frac{1}{6}\tilde{\tau}_5\left(\tilde{\mathbf{D}}\cdot\mathbf{m}^{eq}\right)_5\\-\frac{1}{2}\tilde{\tau}_6\left(\tilde{\mathbf{D}}\cdot\mathbf{m}^{eq}\right)_6-\frac{1}{3}\tau_0\mathbf{\Phi}_0-\frac{1}{3}\tau_4\mathbf{\Phi}_4\\+\frac{1}{6}\tau_5\mathbf{\Phi}_5-\frac{1}{2}\tau_6\mathbf{\Phi}_6\end{array}\right]\\+\frac{\partial}{\partial x}\left[\tilde{\tau}_9\left(\tilde{\mathbf{D}}\cdot\mathbf{m}^{eq}\right)_9-\tau_9\mathbf{\Phi}_9\right]\\+\frac{\partial}{\partial y}\left[\tilde{\tau}_8\left(\tilde{\mathbf{D}}\cdot\mathbf{m}^{eq}\right)_8-\tau_8\mathbf{\Phi}_8\right]\end{array}\right\}+\frac{1}{2}F_z+O\left(\delta t^2\right)\tag{31}$$

where $\tau_k\equiv 1/s_k$ and $\tilde{\tau}_k\equiv 1/s_k-1/2, k=0,1,\ldots,9$. Assuming that the normal and shear stresses are isotropic, the relaxation times related to viscosity are equal $\tilde{\tau}_5=\tilde{\tau}_6=\tilde{\tau}_7=\tilde{\tau}_8=\tilde{\tau}_9$. Applying Eq. (27), Eqs. (29)–(31) can be simplified as:

$$\frac{\partial}{\partial x_i}\frac{\langle u_i\rangle}{\phi}=O\left(\delta t^2\right)\tag{32}$$

$$\frac{\partial}{\partial t}\frac{\langle u_x\rangle}{\phi}+\nabla\cdot\left(\frac{\langle\mathbf{u}\rangle}{\phi}\frac{\langle u_x\rangle}{\phi}\right)=-\frac{1}{\rho_0}\frac{\partial}{\partial x}p+F_x+\frac{1}{3}\nabla\cdot\tilde{\tau}_7\nabla u_x+R_x\delta_t+O\left(\delta t^2\right)\tag{33}$$

$$\frac{\partial}{\partial t}\frac{\langle u_y\rangle}{\phi}+\nabla\cdot\left(\frac{\langle\mathbf{u}\rangle}{\phi}\frac{\langle u_y\rangle}{\phi}\right)=-\frac{1}{\rho_0}\frac{\partial}{\partial y}p+F_y+\frac{1}{3}\nabla\cdot\tilde{\tau}_7\nabla u_y+R_y\delta_t+O\left(\delta t^2\right)\tag{34}$$

$$\frac{\partial}{\partial t}\frac{\langle u_z\rangle}{\phi}+\nabla\cdot\left(\frac{\langle\mathbf{u}\rangle}{\phi}\frac{\langle u_z\rangle}{\phi}\right)=-\frac{1}{\rho_0}\frac{\partial}{\partial z}p+F_z+\frac{1}{3}\nabla\cdot\tilde{\tau}_7\nabla u_z+R_z\delta_t+O\left(\delta t^2\right)\tag{35}$$

where R_x,R_y,R_z are the error terms. They can be written as:

$$\begin{aligned}R_x=&-\frac{2(h_4\tau_4+2h_5\tau_5-\tilde{\tau}_4-2\tilde{\tau}_5)}{3}\frac{\partial}{\partial x}\frac{\langle u_x\rangle}{\phi}F_x-(h_7\tau_7-\tilde{\tau}_7)\frac{\partial}{\partial y}\left(\frac{\langle u_y\rangle}{\phi}F_x+\frac{\langle u_x\rangle}{\phi}F_y\right)+\frac{2(-h_4\tau_4+h_5\tau_5+\tilde{\tau}_4-\tilde{\tau}_5)}{3}\frac{\partial}{\partial x}\\&\times\left(\frac{\langle u_y\rangle}{\phi}F_y+\frac{\langle u_z\rangle}{\phi}F_z\right)-(h_9\tau_9-\tilde{\tau}_9)\frac{\partial}{\partial z}\left(\frac{\langle u_z\rangle}{\phi}F_x+\frac{\langle u_x\rangle}{\phi}F_z\right)\end{aligned}\tag{36}$$

$$\begin{aligned}R_y=&-\frac{2(h_4\tau_4+h_5\tau_5-\tilde{\tau}_4-\tilde{\tau}_5)}{3}\frac{\partial}{\partial y}\frac{\langle u_x\rangle}{\phi}F_x-(h_7\tau_7-\tilde{\tau}_7)\frac{\partial}{\partial x}\left(\frac{\langle u_y\rangle}{\phi}F_x+\frac{\langle u_x\rangle}{\phi}F_y\right)\\&-\frac{(2h_4\tau_4+h_5\tau_5+3h_6\tau_6-2\tilde{\tau}_4-\tilde{\tau}_5-3\tilde{\tau}_6)}{3}\frac{\partial}{\partial y}\left(\frac{\langle u_y\rangle}{\phi}F_y+\frac{\langle u_z\rangle}{\phi}F_z\right)-(h_8\tau_8-\tilde{\tau}_8)\frac{\partial}{\partial z}\left(\frac{\langle u_z\rangle}{\phi}F_y+\frac{\langle u_y\rangle}{\phi}F_z\right)\end{aligned}\tag{37}$$

$$\begin{aligned}R_z=&-\frac{2(h_4\tau_4-h_5\tau_5-\tilde{\tau}_4+\tilde{\tau}_5)}{3}\frac{\partial}{\partial z}\frac{\langle u_x\rangle}{\phi}F_x-(h_8\tau_8-\tilde{\tau}_8)\frac{\partial}{\partial y}\left(\frac{\langle u_z\rangle}{\phi}F_y+\frac{\langle u_y\rangle}{\phi}F_z\right)\\&-\frac{(2h_4\tau_4+h_5\tau_5-3h_6\tau_6-2\tilde{\tau}_4-\tilde{\tau}_5+3\tilde{\tau}_6)}{3}\frac{\partial}{\partial z}\left(\frac{\langle u_y\rangle}{\phi}F_y+\frac{\langle u_z\rangle}{\phi}F_z\right)-(h_9\tau_9-\tilde{\tau}_9)\frac{\partial}{\partial x}\left(\frac{\langle u_x\rangle}{\phi}F_z+\frac{\langle u_z\rangle}{\phi}F_x\right)\end{aligned}\tag{38}$$

To eliminate the effect of the error terms, the following relation is obtained:

$$h_m = 1 - \frac{1}{2\tau_m}, m = 4, 5, ..., 9 \tag{39}$$

Moreover, the relation between the kinematic viscosity ν and relaxation time is given by:

$$\nu = \frac{1}{3}\delta t \tilde{\tau}_7 \tag{40}$$

Finally, the macroscopic governing equations recovered from the novel VANS-LB scheme can be expressed as:

$$\frac{\partial}{\partial x_i}\frac{\langle u_i \rangle}{\phi} = 0 \tag{41}$$

$$\frac{\partial}{\partial t}\frac{\langle u_i \rangle}{\phi} + \frac{\partial}{\partial x_i}\left(\frac{1}{\phi^2}\langle u_i \rangle \langle u_j \rangle\right) = -\frac{1}{\rho_0}\frac{\partial}{\partial x_i}p + \frac{\partial}{\partial x_i}\left(\nu \frac{\partial}{\partial x_j}\frac{\langle u_i \rangle}{\phi}\right) - [CT]_p \tag{42}$$

which are the same as the governing equations Eqs. (1) and (2) proposed at the beginning of this section and prove the correctness of our LB scheme.

2.2.3. Boundary conditions

The non-equilibrium extrapolation scheme is used to reconstruct the distribution functions streaming from the physical boundaries [40].

$$f_\alpha(\mathbf{x}, t + \delta t) = f_\alpha(\mathbf{x} + \mathbf{e}_\alpha \delta t, t + \delta t) + f_\alpha^{eq}[p(\mathbf{x}, t), \langle \mathbf{u}(\mathbf{x}_B, t) \rangle] - f_\alpha^{eq}[p(\mathbf{x}, t), \langle \mathbf{u}(\mathbf{x}, t) \rangle] \tag{43}$$

where $\mathbf{x}_B$ represents the position of the boundary, and the equilibrium distribution function is calculated by Eq. (11).

To study the wave interactions with porous media, the wave generation boundary condition is necessary. The static open boundary wave generator method [41] is applied in our model, and the specific implementation can be found in the study of Liu et al. [19].

For porous media, the single-phase free surface LB model proposed by Thürey [42] is applied with slight modifications. The surface is tracked by the advection function given by Higuera et al. [5]:

$$\frac{\partial \varepsilon}{\partial t} + \frac{\partial}{\partial x_i}\frac{\langle u_i \rangle}{\phi}\varepsilon = 0 \tag{44}$$

where ε is the water fraction at each cell. By using the first-order Euler time differencing scheme, the LB-type water flux Q_α is given by:

$$Q_\alpha = \rho_0 \left[f_\alpha(\mathbf{x} + \mathbf{e}_\alpha \delta t) - f_\beta(\mathbf{x}) \right] c A_\alpha \tag{45}$$

where f_β is the distribution function with the discrete velocity $\mathbf{e}_\beta = -\mathbf{e}_\alpha$, and A_α is the face of the water flux coming through and is defined as:

$$A_\alpha = \begin{cases} \frac{1}{2}(\phi(\mathbf{x}) + \phi(\mathbf{x} + \mathbf{e}_\alpha))\delta x^2 & \text{neighbour is liquid} \\ \frac{1}{2}(\varepsilon(\mathbf{x}) + \varepsilon(\mathbf{x} + \mathbf{e}_\alpha))\delta x^2 & \text{neighbour is surface} \\ 0.0 & \text{neighbour is gas} \end{cases} \tag{46}$$

where $A_\alpha = \delta x^2$ in the original model of Thürey [42] when the neighbour is fluid with the absence of porous media. Then the free surface Körner scheme [43] is adopted to reconstruct the unknown distribution function at the free surface boundary. Detailed information can be found in the work of Liu et al. [19].

3. Calibration of the resistance parameters

The novel LB scheme proposed in Section 2 requires a calibration of the porous medium resistance parameters. The most common dam break case is used. The experimental setup and numerical results are discussed in this section.

3.1. Experimental and numerical setup

To calibrate the porous resistance parameters, experiments of dam-break waves interacting with porous structures conducted by Lin [44] are used. The experiments are carried out in a fish tank with a size of 0.892 m × 0.58 m × 0.44 m. Two kinds of porous structures (made by crushed rocks or glass beads) with a size of 0.29 m × 0.37 m × 0.44 m are placed at x = 0.3-0.59 m. The nominal diameter (D_{50}) and porosity (ϕ) of the two kinds of porous media are 1.59 cm, 0.49 and 0.3 cm, 0.39, respectively. A gate with a thickness of 2 cm is placed in front of the porous structure. Three initial water levels (15 cm, 25 cm and 35 cm) on the front (left) side of the gate are considered. At the beginning of the experiment, the gate is

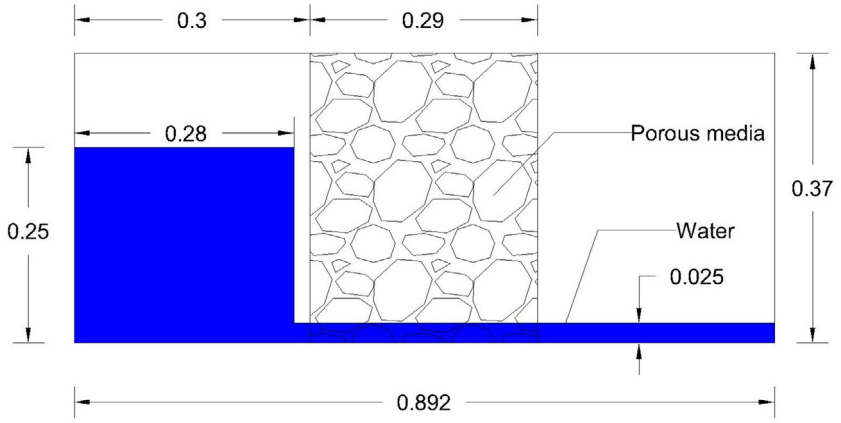

Fig. 1. Numerical setup for porous dam-breaking (Unit: m).

pulled up within 0.1 s and the water is released. The free surface elevation both inside and outside of the porous structure is recorded by a camera during the whole experiment. More details about the experiments can be found in the work of Lin [44].

The numerical setup is shown in Fig. 1. Although the computational domain can be set up in two-dimensional such as Liu et al. [1] and Ren et al. [8], we use a three-dimensional domain in this test case to validate the three-dimensional VANS-LB model. To reduce the total grid number, the height of the numerical domain is 0.37 m, the same as the height of the porous structure. The initial water level is set as 25 cm to ensure that no water splashes over the porous structure. A gap of 2 cm thickness between the initial water and the porous structure represents the gate in the experiments. Only the dam-break wave passing through the porous structure of crushed rocks is used to calibrate the porous resistance parameters, as the pore Reynold number (Re), defined by Lin [44], for this case is in the range of $O(10^3)$, which pertains to the fully turbulent regime [45]. According to Lin [44] and del Jesus et al. [4], the linear frictional force is negligibly small compared with the nonlinear frictional force when the flow is fully turbulent in porous media. Therefore, only the nonlinear friction parameter β is calibrated for this model. For the linear friction parameter α and added mass parameter γ, the values of $\alpha = 10000$, $\gamma = 0.34$, as suggested by Burcharth and Andersen [46], are adopted. The characteristic time scale of the crushed rock case T_0 (the time for water flowing through the porous structure) is set as 1.0, as suggested by Lin [44], and used to calculate the KC number. The free slip boundary condition is applied on all the walls, and the zero-pressure boundary condition is employed on the free surface. The Smagorinsky coefficient C_s in the large eddy simulation is 0.15, as suggested by Hu et al. [3].

First, the grid size dependence on numerical solutions is investigated using three different grid sizes. The grid sizes are 0.01 m, 0.005 m and 0.0025 m. Then, the model is calibrated by comparing the numerical simulation results with different nonlinear friction parameters ($\beta = 1.5$, 3.0, 6.0) with the measured data from the experiment. The absolute errors are also analysed to choose the best fit parameter. Finally, the numerical result with the best fit parameter at a water level gauge is compared with the experimental data and other numerical model solutions. Furthermore, the velocity vectors and vorticity are shown to prove that the results are reasonable.

3.2. Simulation results

The first step of the calibration is the study of the grid size dependence. In the simulation, the Mach number (Ma), which represents the incompressibility and numerical stability in the LBM is set as 0.064 (suggested to be no larger than 0.15 by He and Luo [47]). The initial values of the friction parameters are set as the suggestion of Burcharth and Andersen [46]. The total grid numbers for the three grid sizes are 144,892, 1,159,136 and 9,299,136. The simulation duration is 3.0 s. Fig. 2 shows that there is no significant difference between the middle and fine grids inside or outside the porous structure. The coarsest grid result has a small deviation both upstream and downstream of the porous medium. Therefore, to reduce the computational time and maintain accuracy, the middle grid is used for the rest of calibration case.

The influence of the porous medium in the experiment is modelled by the porous medium friction force in the numerical simulation. Many forms of empirical formulas are available to describe the frictional force; these formulas include different friction parameters. These parameters depend on the flow regime and porous medium characteristics, such as the Reynolds number, porosity, shape and grade of the porous medium. These aspects are not completely understood and need to be calibrated for different models. Engelund's formula, which can account for the variation in the porous medium characteristics, is used in this model. Although calibration procedures were carried out for the previous 2D or 3D RANS models [4,5,48], the friction parameters for the LB model using LES still need to be calibrated.

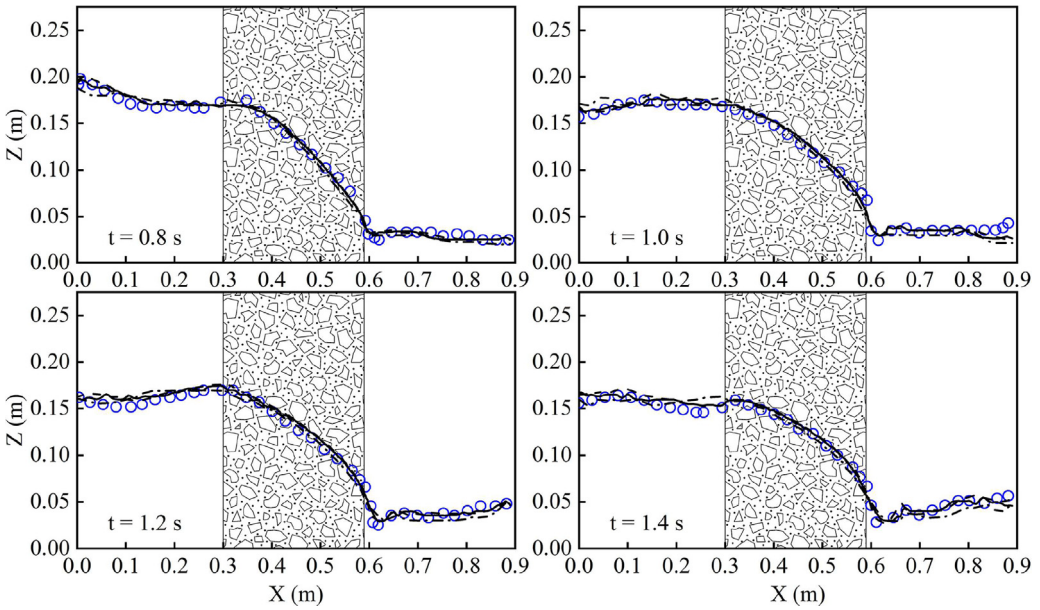

Fig. 2. Grid size dependence. Experimental data (circles) [44]. $\alpha = 10000$, $\beta = 3$ for numerical simulations, coarse grid $\delta x = 0.01$ m (dash-dotted lines), middle grid $\delta x = 0.005$ m (solid lines), fine grid $\delta x = 0.0025$ m (dashed lines).

Table 1
Error analysis for the nonlinear friction parameter $\beta = 1.5$.

t(s)	0.8	1.0	1.2	1.4
Max	1.67	1.77	2.03	2.50
Area	50.1	45.6	49.1	58.3
Mean	9.5	11.0	12.2	11.5

Table 2
Error analysis for the nonlinear friction parameter $\beta = 3.0$.

t(s)	0.8	1.0	1.2	1.4
Max	1.08	1.57	0.91	1.20
Area	32.2	32.2	31.9	32.0
Mean	5.8	6.9	5.7	5.5

The key parameter β is studied while the linear friction parameter α is kept equal to 10000. Fig. 3 shows a comparison between the free surface of the numerical results with different nonlinear parameters and the experimental data. The experimental data are represented by circles. The dashed lines represent $\beta = 1.5$. The solid lines represent $\beta = 3.0$. The dash-dotted lines represent $\beta = 6.0$. Apart from $t = 0.0$ s to $t = 0.4$ s, the numerical simulation of $\beta = 3.0$ seems to be the best result compared with the experimental data. Obvious error occurred in the early stage when the water is released because that the gate between the porous structure and water is manually moved upward at the beginning of the experiment (approximately 0.1 s). This means that the water is accelerated only at the bottom at first. However, in the numerical simulation, the gate between the porous structure and water is simplified by a gap, which causes the water to move slower at the bottom and faster at the top in the early stage.

To further analyse the error between the numerical results and experimental data, several error indicators are introduced. The absolute error is given as $\Delta_i = h_{i,sim} - h_{i,\exp}$, where $h_{i,sim}$, $h_{i,\exp}$ are the free surface elevation at the same location in the simulation and experiment, respectively. Therefore, the maximum absolute error is $\Delta_{\max} = \max(|\Delta_i|)$. The area under the absolute error curve is given as $\Delta_{area} = \int |\Delta(x)| dx$. The error rate is $\Delta_{i,r} = (h_{i,sim} - h_{i,\exp})/h_{i,\exp} \times 100\%$ and the mean error rate is $\Delta_{mean} = \sum_{i=1}^{N} \Delta_{i,r}/N$. The absolute errors between numerical simulations with different parameters and experimental data for choosing the best fit parameter are shown in Fig. 4, and the maximum absolute error, the area under the absolute error curve and the mean error rate for different parameters are shown in Tables 1–3. The duration for calculating the error is chosen as the range of $t = 0.8$-1.4 s so that the error is not influenced by the opening of the gate at the beginning or water reflection at the end. Fig. 4 shows that the blue-circle line is closer to zero than the other two lines in the whole domain, which means that the absolute error of $\beta = 3.0$ is the smallest among the parameters. The same conclusion can be obtained from Tables 1–3. The maximum absolute error, area under the curve and mean error rate of $\beta = 3.0$ are 1.57 cm, 32.2 cm^2

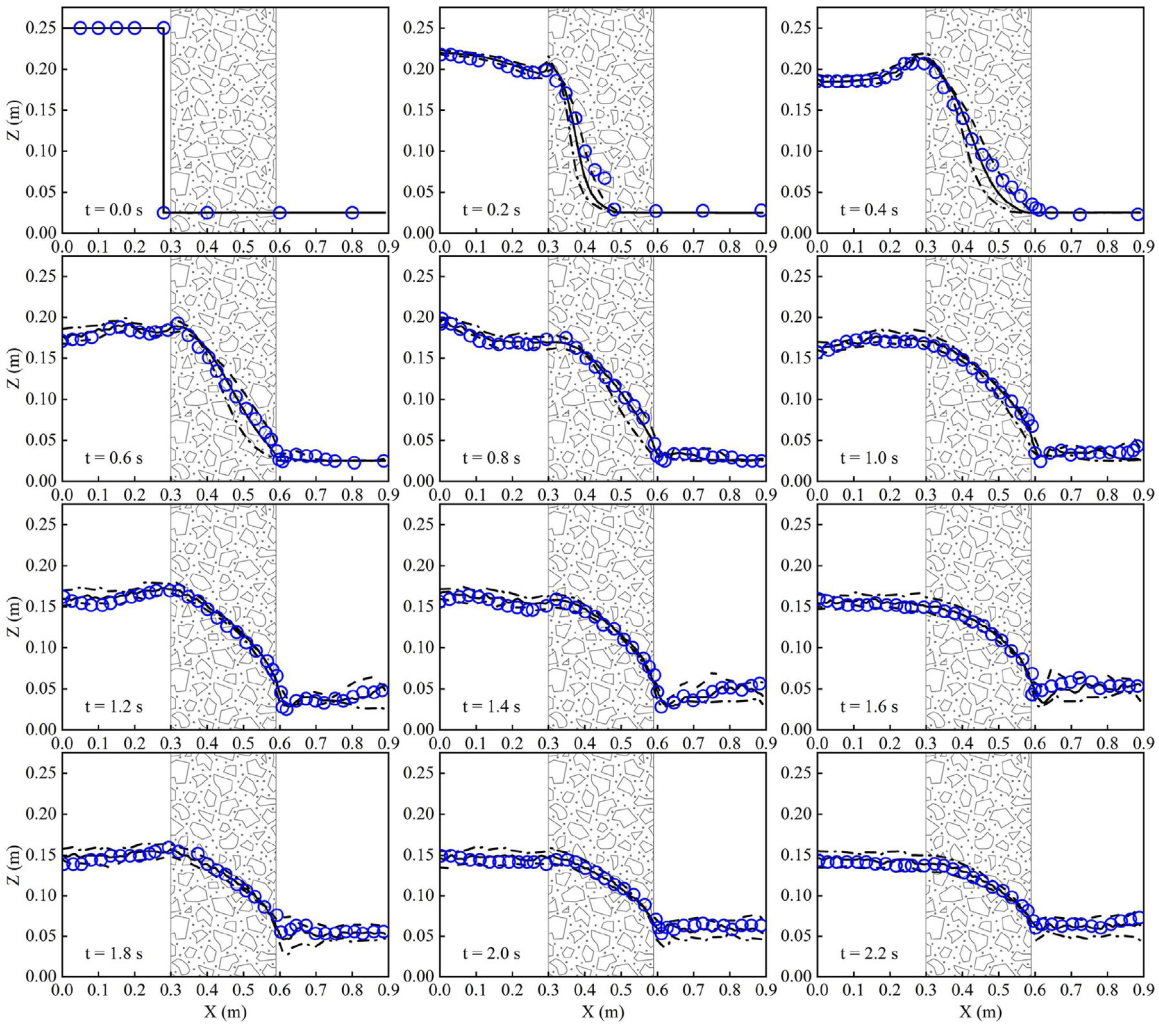

Fig. 3. Nonlinear friction parameter β calibration for the crushed stone case. Experimental data (circles) [44]. Numerical simulation results of different nonlinear friction parameters β: 1.5 (dashed lines), 3 (solid lines) and 6 (dash-dotted lines).

Table 3
Error analysis for the nonlinear friction parameter $\beta = 6.0$.

t(s)	0.8	1.0	1.2	1.4
Max	3.05	2.97	2.23	2.03
Area	76.9	78.6	82.0	83.3
Mean	11.4	14.0	12.7	11.8

and 6.9%, compared with the 2.50 cm, 58.3 cm^2, and 12.2 % of $\beta = 1.5$ and 3.05 cm, 83.3 cm^2, and 14.0 % of $\beta = 6.0$ in the time duration of $t = 0.8$-1.4 s, respectively. Therefore, the best fit nonlinear friction parameter is $\beta = 3.0$, which is used for the rest of the simulation. Moreover, the total mass is calculated by recording the volume of water phase in the lattice unit before and after the simulation. The mass loss is 2.1%, mainly because the single-phase volume-of-fluid (VOF) model removes the splashing droplet if a liquid lattice is surrounded by the gas lattice in all directions. This aspect does not significantly affect the simulation result. Another interesting fact shown in Fig. 4 is that both the $\beta = 1.5$ and $\beta = 6.0$ cases have similar absolute error patterns in different time stages. In the $\beta = 1.5$ case, the surface elevation upstream of the porous structure is always underestimated, and the surface elevation downstream is overestimated. In the $\beta = 6.0$ case, the opposite trend is observed. This is because a smaller parameter underestimates the friction force exerted by porous media and causes more water flow through the structure, and the opposite is true for a larger parameter.

The numerical result with the best fit parameter for surface elevation at $x = 0.445$ m during the time history of $t = 0.8$-1.4 s is compared with other numerical results, such as the finite difference model [44] and SPH model [8]. Fig. 5 shows

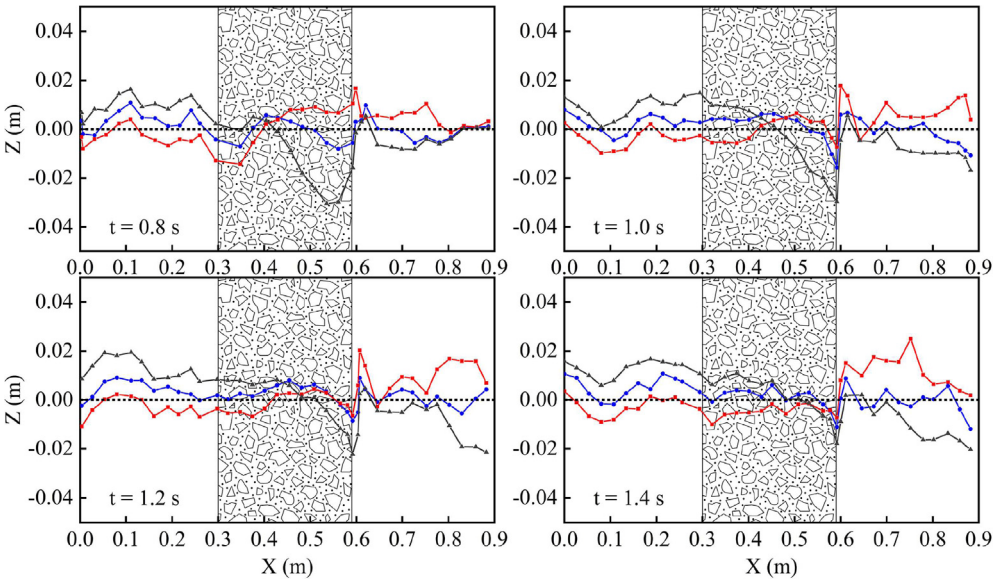

Fig. 4. Absolute errors between the surface elevations of the numerical simulations and experimental data. Absolute errors of different nonlinear friction parameters (β): 1.5 (red-square line), 3 (blue-circle line), and 6 (grey-triangle line).

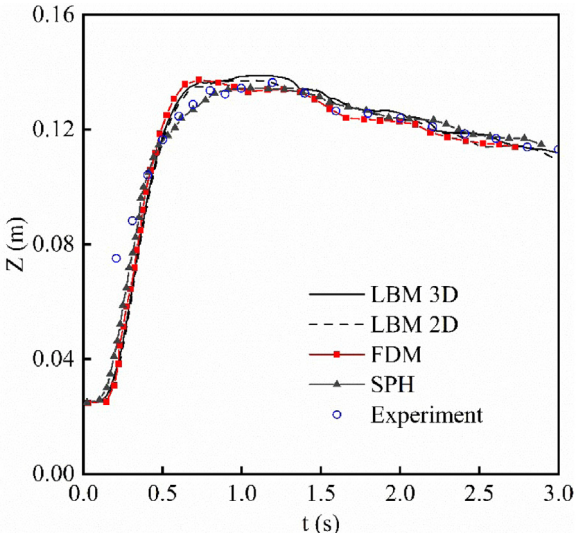

Fig. 5. Comparison of the time history free surface elevation at $x = 0.445$ m from the experimental data [44], FDM results [44] and SPH method results [8].

that all the models lack accuracy at the beginning due to different water release methods. All the models achieve similar curves that agree well with the experimental data. The LBM model shows nearly the same accuracy as the finite difference model and slightly lower accuracy than the SPH model. In fact, both the LBM model and the finite difference model use the same VOF model to capture the free surface, and this model is slightly less accurate than the method used in the SPH model. However, this error can be tolerated in most cases.

For more details, Fig. 6 shows the velocity vectors and vorticity at different time steps. At the beginning of the simulation ($t = 0.2$ s), the dam-break water strongly impacts the porous structure. The water near the porous structure has a horizontal velocity of approximately 0.2 m/s, while the water near the left wall primarily moves vertically. The largest vorticity occurs at the top of the water and porous structure interface. Phenomena such as wave breaking and wave reflection occur at this location. At $t = 0.6$ s, part of the water continuously seeps into the porous medium, and part of the water reflected by the porous structure moves towards the left wall. At the characteristic time ($t = 1.0$ s), the water begins seeping out of the porous medium. The velocity reaches 0.15-0.25 m/s downstream of the porous structure. Due to the difference in velocity, the flow region narrows downstream of the porous structure at approximately $x = 0.6$-0.62 m. At $t = 1.4$ s, the water keeps

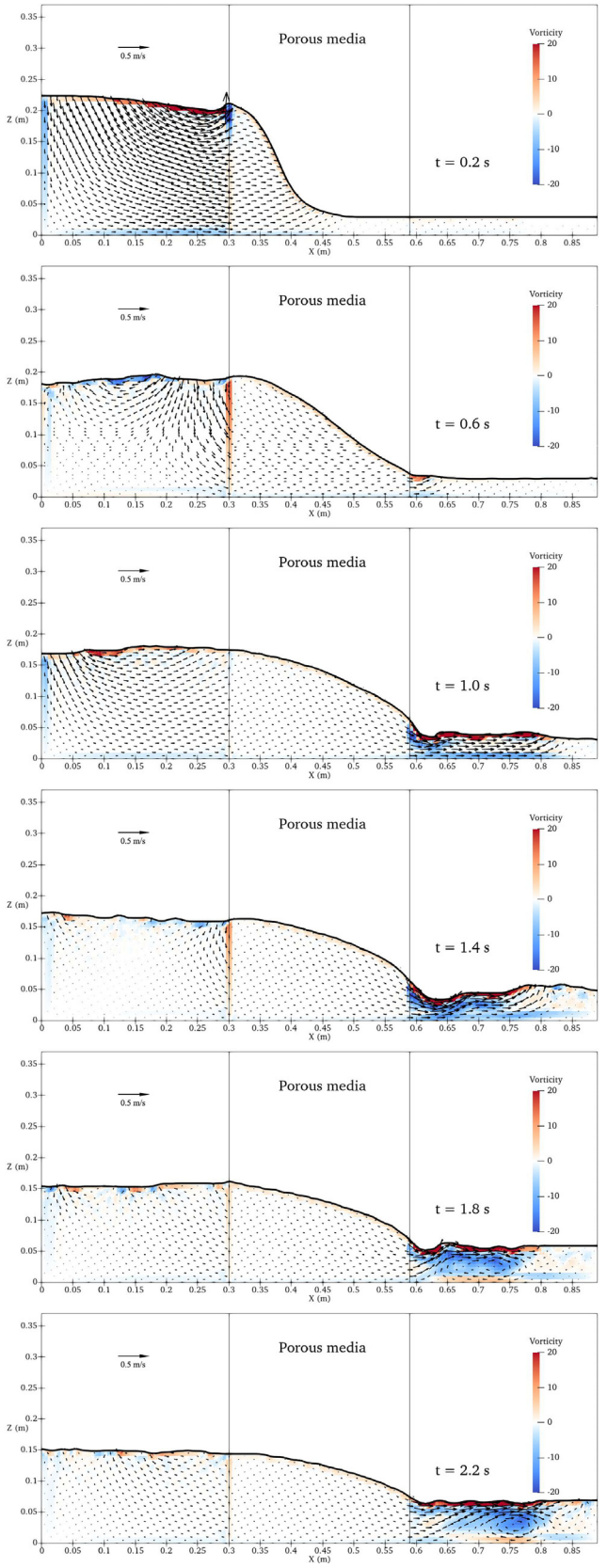

Fig. 6. Velocity vectors and vorticity contours at different time steps.

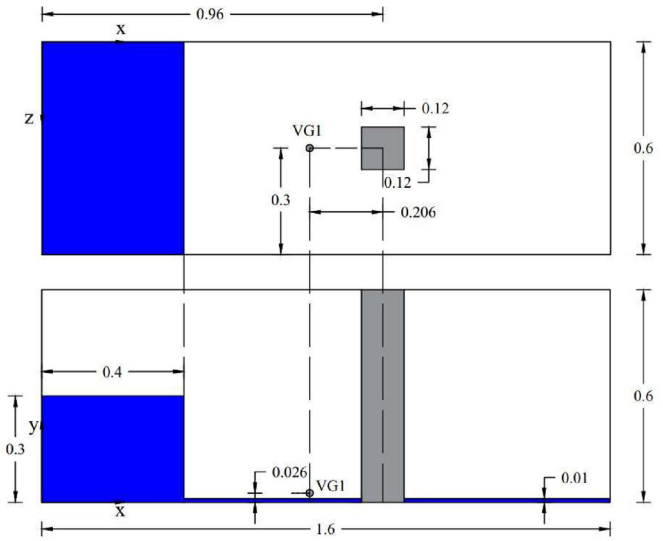

Fig. 7. Experimental and numerical setups for dam-break waves interacting with a square prism. Upper panel: top view. Lower panel: front view (Unit: m).

seeping out of the porous media, and the narrow region develops to $x = 0.6$-0.65 m; the vorticity is also the largest in this area. A small wave occurs downstream of the porous structure and moves towards the right wall. At $t = 1.8$ s, as the water keeps seeping, the water level reaches approximately 0.06 m. The wave reflected by the right wall interacts with the seeping water, which causes circulation in the region of $x = 0.65$-0.75 m. At the end of the simulation ($t = 2.2$ s), the water level reaches 0.07 m downstream. As the water level difference is relatively small, the seeping process slows, and the water surface becomes static downstream.

In conclusion, the friction parameters $\alpha = 10000$, $\beta = 3$ exhibit the best performance in the simulation. The newly derived VANS-LB scheme has the ability to simulate porous flow in this preliminary model assessment.

4. Validations of the 3D VANS-LB model

In this section, further validation work is carried out to verify that the VANS-LB model has the ability to simulate the interaction of waves and porous structures. First, 3D highly unsteady dam-break waves interacting with both solid and porous structures are considered. In this case, phenomena such as wave breaking occur; wave breaking is a significant process in the design of coastal structures. The velocity and the net force are used for comparison with the experiment. Then, both solitary wave and cnoidal waves interacting with a permeable vertical breakwater are applied to validate the model and to reproduce the wave reflection, diffraction and transmission processes in the numerical simulation. Finally, the validation is extended for the interaction of regular waves and a rubble mound breakwater with multi-layered porous media to prove that the model is capable of reproducing spatially varying porous structures.

4.1. 3D dam-break waves impacting a solid or permeable prism

4.1.1. Experimental and numerical setup

The first experiment chosen to validate the VANS-LB model is a 3D dam-break wave impacting a solid prism; this experiment was carried out by Wu [49]. The laboratory and numerical setups are shown in Fig. 7. The tank is 1.6 m long, 0.6 m wide and 0.6 m high. The centre of the prism is placed at (0.96, 0.3, 0.3). The prism is 0.12 m long, 0.12 m wide and 0.6 m high. The initial water volume stored in the left side of the tank is 0.4 m long, 0.6 m wide and 0.3 m high. Water is placed in the rest of the tank to a height of 1 cm. A laser Doppler velocimetry and a velocity gauge are placed 0.146 m upstream of the left face of the structure and 0.026 m above the bottom of the tank in the laboratory experiment and numerical simulation, respectively. The force is measured using a load cell in the experiment. The numerical force is measured through pressure integration on the front and back faces of the structure and neglecting the shear force which is 1% of the normal force according to Wu [49]. More experimental descriptions can be found in the work of Wu [49]. Only the solid prism case is carried out in the experiment. However, the porous prism case is also calculated by the FVM model [50] and SPH model [12]. Therefore, both the solid and porous cases are used to validate the new model. The porosity and nominal diameter of the porous media are 0.5 and 0.015 m, respectively. The porous medium friction parameters used here are the same as those in the calibration case ($\alpha = 10000$, $\beta = 3$, $\gamma = 0.34$). The free-slip boundary condition is imposed on all the solid boundaries. On the free surface, the zero-pressure boundary condition is employed. The Smagorinsky parameter is set

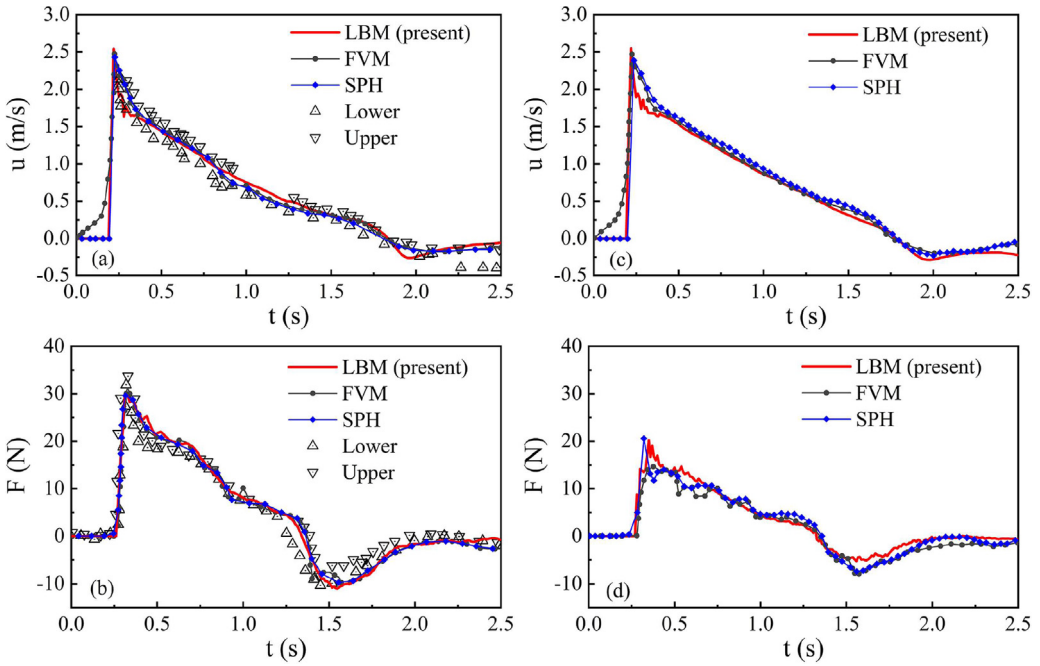

Fig. 8. Comparisons of the time history velocity at a specific point and net force on a solid or porous square prism of the experimental data [49], FVM results [50] and SPH results [12]. Left column: solid case, (a) velocity, (b) net force. Right column: porous case, (c) velocity, (d) net force.

to 0.1. A uniform grid with grid length $\delta x = 0.75$ cm in all directions is used in both the solid and porous cases. The total grid number is 1,363,200, and a period of 2.5 s is simulated.

4.1.2. Simulation results

The numerical results of the VANS-LB model are compared with the experimental data and numerical results of the FVM model and SPH model in Fig. 8. In the left panel, both the experimental data and numerical results of the FVM model and SPH model are available for the solid prism case. Different series of experimental data are shown as the upper and lower envelopes in Fig. 8(a) and (b). In the right panel, only the numerical results of the FVM model and SPH model are available to validate the LBM model for the porous prism case. Fig. 8(a) shows that the velocity predicted by the LBM model is nearly always in the envelope of the experimental data and agrees well with other numerical results. The slight difference between the LBM model and FVM model at the beginning of the simulation mainly occurs because the single-phase VOF method is used in the LBM model, while the two-phase VOF method is used in the FVM model. In the early stage of the simulation, a trapped air phenomenon occurs, and the velocity of the air is omitted by the single-phase free surface model, which results in slightly lower accuracy. Applying a two-phase free surface model in the LBM model will be performed in our future work. Fig. 8(b) shows that the pressure integration method used in the LBM model to calculate the net force can obtain results similar to those of the FVM model and SPH model. All the numerical models underestimate the peak of the force at time $t = 0.3$ s by 5% and overestimate the force at the period of $t = 0.4$-0.7 s by approximately 7%. This phenomenon occurs because different ways of releasing water are applied in the laboratory experiments and numerical simulations. Although the LBM model predicts the peak of the negative force, it does not capture the peak position in time (delayed by approximately 0.1 s). Nevertheless, the LBM model still has the best performance of the models regarding the prediction of the negative force. Fig. 8(c) shows the velocity predicted by different models in the porous prism case. Except for the difference at the beginning, the three different models can achieve similar results. The reason for the difference is the same as that in the solid case. Comparing Fig. 8(a) and (c) shows that the peak position and the peak value of the velocity are not affected by the prism type. Due to part of the water seeping into the permeable structure, less water is bounced back by the prism which yields inverse velocity in the porous case. Therefore, the velocity in the porous prism case is higher than that in solid prism case after the peak. Fig. 8(d) shows the net force calculated by different models for the porous prism case. Different models exhibit the same trend for the versions of the net force. The largest net force occurs at the same time as that in the solid case. However, the peak value of the force on the porous structure is 20 N, while it is 30 N on the solid structure. Both the LBM model and SPH model predict a larger net force when the flow first impacts the porous structure than the FVM model. This is probably due to the presence of air in the FVM model. When the water is released, the air in front of the water is pushed towards the porous media, and the porous resistance force is first imposed on the air. Thus, the water 'realizes' the existence of the porous medium when the water is released in the FVM model. However, in the LBM model and SPH model, water 'realizes' the existence of the porous medium only when water impacts the structure. This aspect

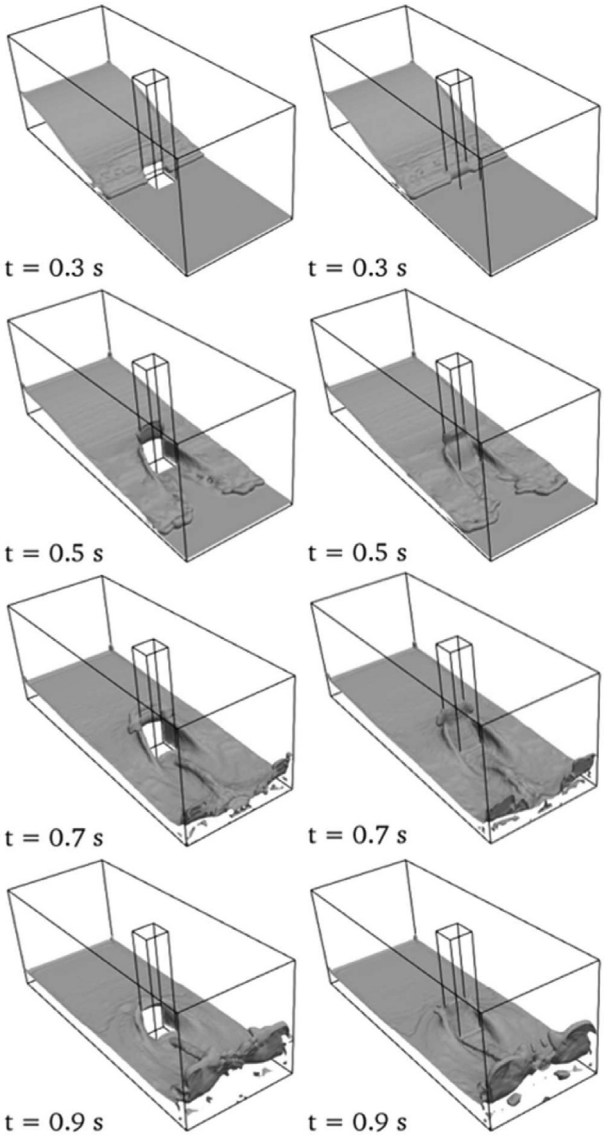

Fig. 9. Comparisons of the free surface elevation. Left column: solid case. Right column: porous case.

may lead to a larger predicted net force in the early stage. Moreover, the total mass is calculated, and the mass losses for the solid and porous prism cases are 4% and 1.4%, respectively. The solid prism case involves a larger mass loss owing to the more violent breaking phenomenon in this case than that in the porous prism case.

Figs. 9 and 10 show the free surface elevation over the whole domain and a slice at $y = 0.3$m for both the solid and porous prism cases. The free surface is represented by the isoline of the volume fraction of the water phase $\varepsilon = 0.5$. At $t = 0.3$ s, the water bore reaches the front face of the prism. No clear difference can be found in the upstream and downstream surfaces of the structure except for the water beginning to seep into the porous media, while no water can enter the solid prism. Trapped air can be found in both the solid and porous cases at slices of $y = 0.3$m. At $t = 0.5$ s, the water splashes higher at the front face of the solid prism. The water keeps seeping in the porous media, which causes a lower rise of water in the front face and both side faces. Furthermore, the water begins seeping out of the middle of the porous prism, while the diffraction water does not reach this location in the solid case. As the water front is moving, a more obviously different flow pattern can be found both upstream and downstream of the prism. At $t = 0.7$ s, the water starts to be reflected by the solid prism, while it still rises at the front face of the porous prism due to the slower inverse velocity. A clear three-dimensional surface pattern appears downstream of the prism. The water elevation is slightly higher close to the back middle of the prism in the porous case because of seepage flow. However, the diffracted water moves faster and collides more violently in the middle of the downstream region, causing a higher water level. As the flow reaches the right

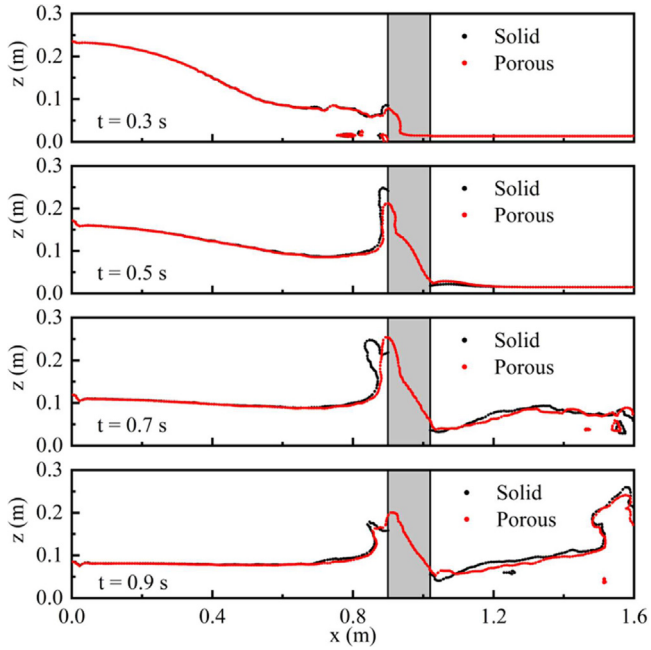

Fig. 10. Comparisons of the free surface elevation at the slice of $y = 0.3$ m.

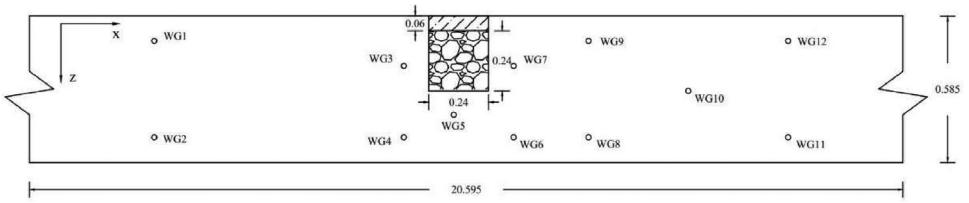

Fig. 11. Sketch of the wave flume and wave gauge position near the porous structure (Unit: m).

Table 4
Wave gauge positions.

Gauge number	X (m)	Z (m)	Gauge number	X (m)	Z (m)
WG1	9.757	0.100	WG7	11.257	0.200
WG2	9.757	0.485	WG8	11.557	0.485
WG3	10.757	0.200	WG9	11.557	0.100
WG4	10.757	0.485	WG10	11.957	0.300
WG5	10.957	0.395	WG11	12.357	0.485
WG6	11.257	0.485	WG12	12.357	0.100

boundary, air is trapped at the bottom of the tank in both cases. At $t = 0.9$ s, the water is reflected by the right boundary and a higher water elevation in downstream and higher run-up at the boundary are observed in the solid prism case.

4.2. 3D solitary or regular wave interactions with a permeable vertical breakwater

4.2.1. Experimental and numerical setups

To investigate the capability of the VANS-LB model further, the experimental data of wave interaction with vertical breakwater [50] is used. Both impermeable and permeable breakwaters are investigated in the experiment. For the permeable breakwater case, a porous structure that is 0.24 m long, 0.24 m wide and 0.70 m high is placed in the wave flume, as shown in Fig. 11. Impervious Plexiglas 6 cm wide is used to attach the porous structure in the experiment. The porous structure is made of stones with a mean diameter of 0.83 cm and a porosity of 0.48. Twelve wave gauges are placed near the porous structure to measure the surface elevations. The wave gauge positions are shown in Table 4.

The solitary wave and cnoidal wave experimental cases used for the numerical simulation are case 2.1 and case 2.2.3 in Section 7.1.2 of the report of del Jesus [51]. The wave conditions are shown in Table 5. The Reynolds number in the experiments is of the order of $O(10^3)$; therefore, the porous friction parameters are chosen to be the same as those in the

Table 5
Wave conditions.

Case	Water depth h (m)	Wave height H (m)	Wave period T (s)
Solitary wave	0.35	0.06	/
Cnoidal wave	0.25	0.06	2.0

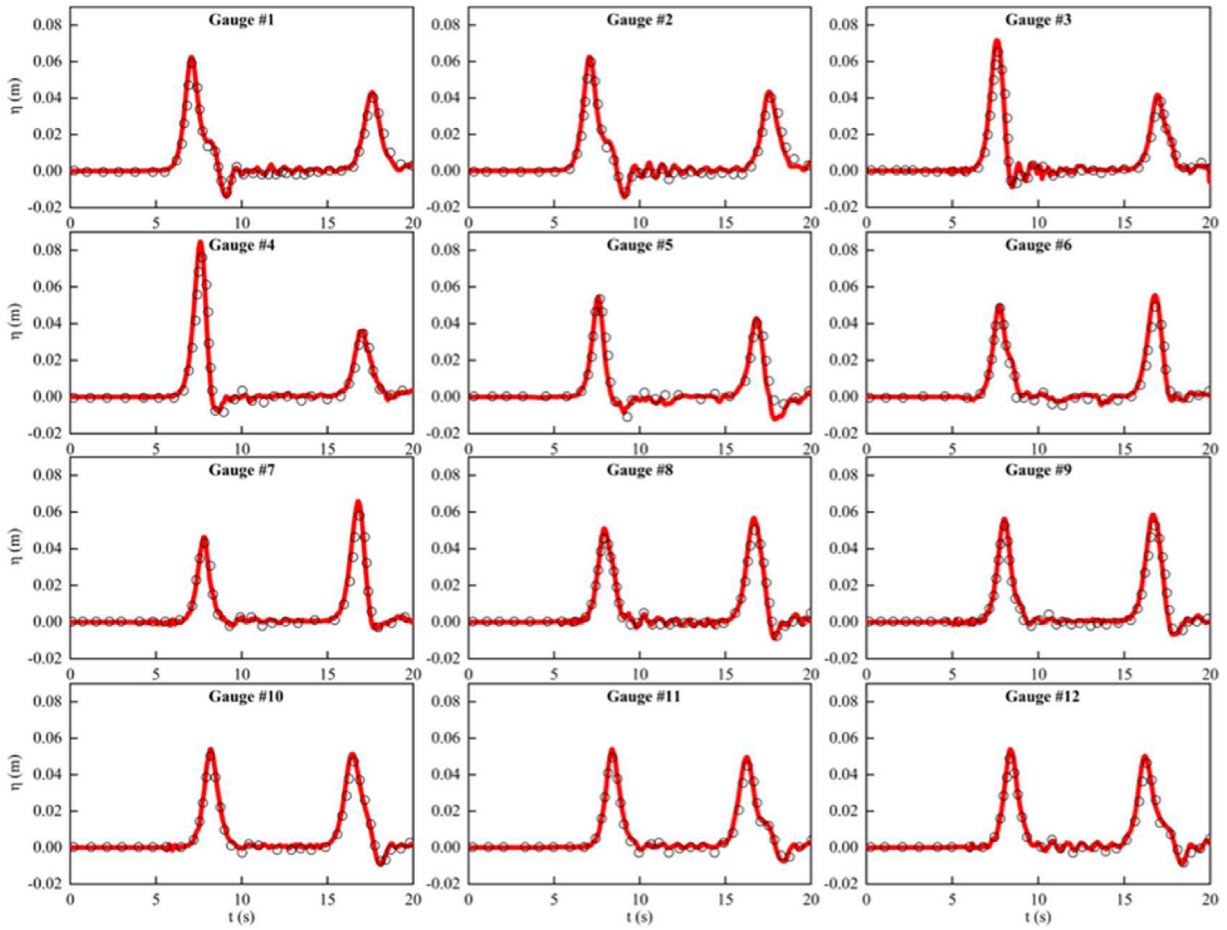

Fig. 12. Comparisons of the numerical results and experimental data for the solitary wave case. The red lines represent the numerical results. The black circles represent the experimental data [50].

crushed rock calibration case, $\alpha = 10000$, $\beta = 3.0$, $\gamma = 0.34$. The Smagorinsky parameter is equal to 0.15. A slip boundary condition is used on both sidewalls. A nonslip boundary condition is adopted on the rest of the boundaries. The wave gauge sampling frequency is 100 Hz. The numerical domain is the same as the experimental layout except for the height of the wave flume. The heights of the numerical domain are reduced to 0.48 m and 0.375 m for the solitary and cnoidal wave cases, respectively, to reduce the total grid number. A uniform grid with grid length $\delta x = 0.375$ cm in all directions which is $H_{LB} = H/\delta x = 16$ is used in both the solitary and cnoidal wave cases, as the sensitivity analysis has already been performed by Liu et al. [19] for the impermeable breakwater simulation case. The total grid numbers are 110,822,400 and 86,580,000. The total simulation duration is 24 s. These test cases have been run on Tianhe-3 prototype with Phytium MT2000+/32@2.2 GHz processers using 1600 CPU cores, and it takes 12.11 h and 9.62 h to complete the simulations for the solitary and cnoidal wave cases, respectively.

4.2.2. Simulation results

Fig. 12 shows the numerical results of the free surface elevation compared with the experimental data. The discrepancy rates of the wave crest between the simulation result and experimental data are defined to be the same as those used by Liu et al. [19], as $\Delta_{cr} = |\eta_{s,\max} - \eta_{m,\max}|/H \times 100\%$. The incident and reflection wave crest discrepancy rates of the 12 gauges ($\Delta_{i,cr}$, $\Delta_{r,cr}$) are shown in Table 6. The mean difference rates of the incident and reflection wave crests are 6.3% and 7.0%, respectively. Gauges 3 and 4 have a slightly higher incident wave crest. This phenomenon occurs because the porous media

Table 6
The discrepancy rates of the wave crest in the solitary wave case.

Gauge number	$\Delta_{i,\ cr}$ (%)	$\Delta_{r,\ cr}$ (%)	Gauge number	$\Delta_{i,\ cr}$ (%)	$\Delta_{r,\ cr}$ (%)
WG1	5.4	4.9	WG7	5.0	11.3
WG2	4.6	5.3	WG8	6.6	10.5
WG3	9.5	5.9	WG9	5.4	9.7
WG4	11.0	1.9	WG10	3.7	6.8
WG5	1.3	4.1	WG11	10.3	7.9
WG6	2.5	9.4	WG12	8.1	5.9

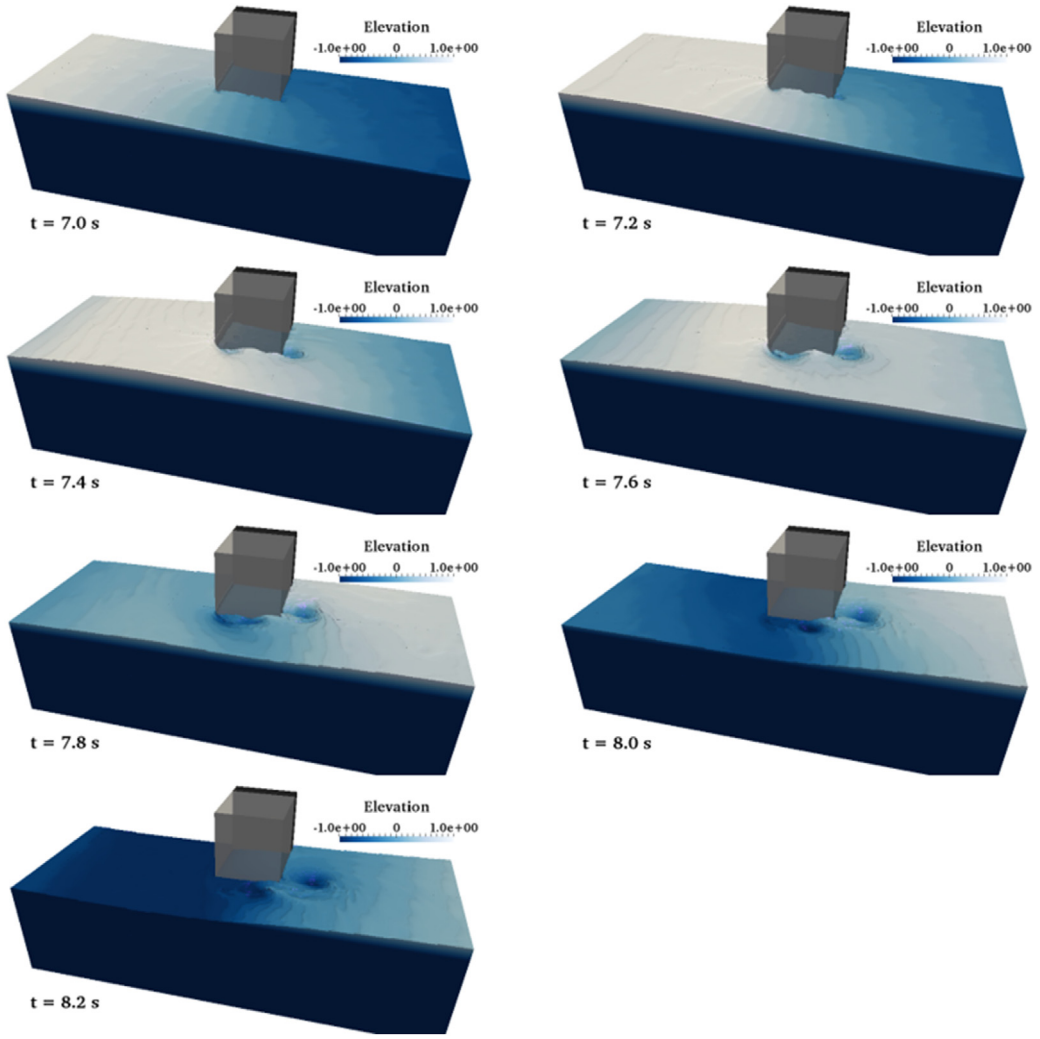

Fig. 13. Solitary wave transformation near the permeable vertical breakwater.

closure is a compromise between the efficiency and accuracy. The media material, shape of the solid skeleton and surface roughness cannot be reflected in the closure, but the flow field near the porous structure is influenced by these aspects, and a discrepancy is inevitably introduced. However, in the whole computational domain, we believe that the error is acceptable, and the present porous media closure is effective.

Fig. 13 also shows the time variation of the wave elevation when the solitary wave interacts with the porous structure. From $t = 7.0$ s to $t = 7.2$ s, the solitary wave crest arrives in front of the porous structure, which causes a pressure difference between the front and back faces of the porous media. From $t = 7.4$ s to $t = 7.6$ s, the solitary wave interacts violently with the porous structure. Wave reflection, diffraction and seepage in the porous medium occur at the same time. Two obvious vortices appear at the corner of the porous structure due to wave diffraction. Small ripples generated by seepage flow emerge close to the back face of the porous structure. From $t = 7.8$ s to $t = 8.2$ s, the solitary wave leaves the porous

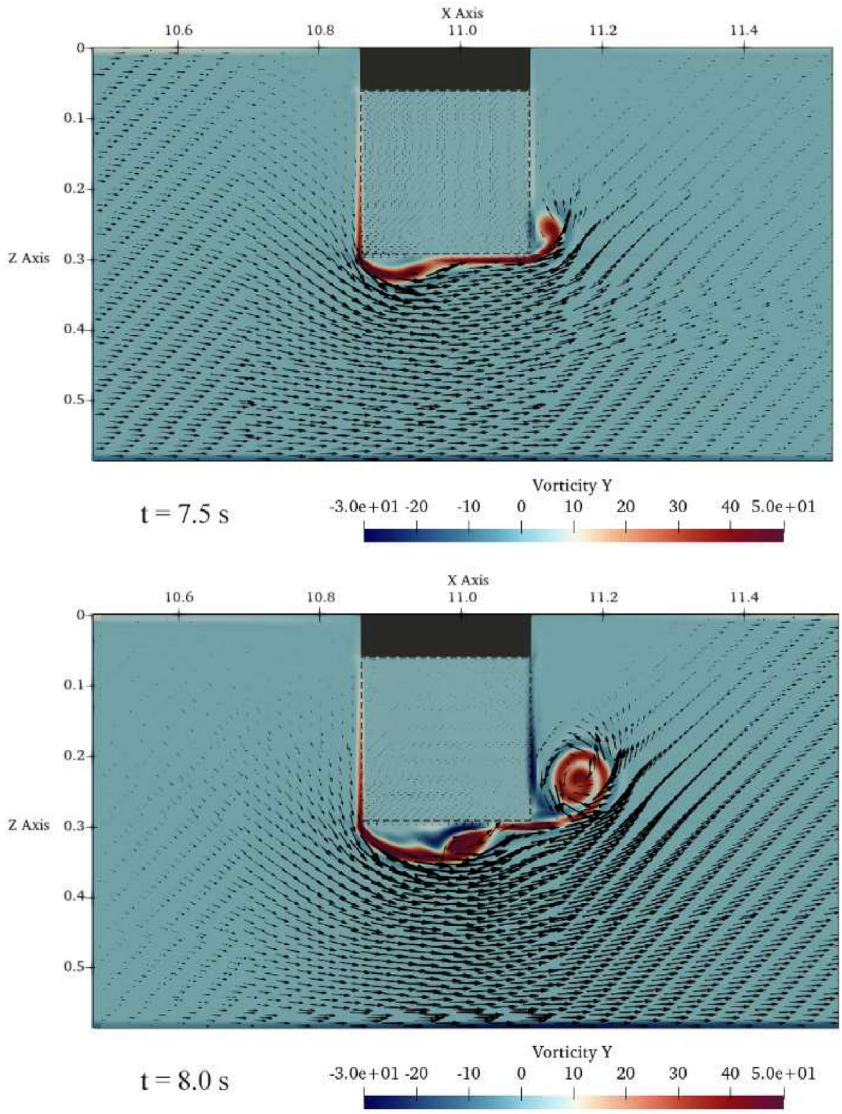

Fig. 14. Velocity vectors and vorticity at slice Y = 0.2 m for the solitary wave case.

structure. Vortices at the corner still exist, while the water elevation becomes calm and the head difference gradually vanishes in the porous medium. The water elevations both inside and outside the porous structure become still water levels. Moreover, at t = 7.5 s and t = 8.0 s, the velocity vectors and vorticity are shown at an X-Z plane Y = 0.2 m in Fig. 14. The physics of solitary wave transformation near the porous is well captured. Most of the wave energy passes around the vertical breakwater by wave diffraction, and large vorticity appears at the corners of the structure.

Fig. 15 shows a comparison of our model with the experimental data and simulation result of the FVM model in the cnoidal wave case [50]. The first 10 of 12 wave gauges are chosen because the experimental data of these gauges are available in Lara et al. [50]. Only the results of t = 0-17 s are shown in Fig. 15 because the outflow boundary condition is not mentioned in Lara et al. [50]. However, the wave elevation is sensitive to the phase and height of the reflection wave, which rely on the outflow boundary in the experiment. Therefore, with the difficulty of confirming which kind of outflow boundary should be implemented in the numerical study, only the first five waves, which are not affected by the reflection waves yet, are used to evaluate the model accuracy. The discrepancy rates of the wave crests are calculated as the average of the first five waves. The results are shown in Table 7. The mean difference rates of the wave crests for the LBM model and FVM model are 6.85% and 6.87%, which demonstrates that the present VANS-LB model can simulate the cnoidal wave interaction with the porous structure with an accuracy comparable to that of the FVM model. For wave gauges 1 and 2, the discrepancies pertain to the first wave, corresponding to the error of 13.1% and 15.3%, respectively. A likely reason is the wave generation difference between the numerical model and experiment. As shown in Fig. 15, similar discrepancies of 14.6% and

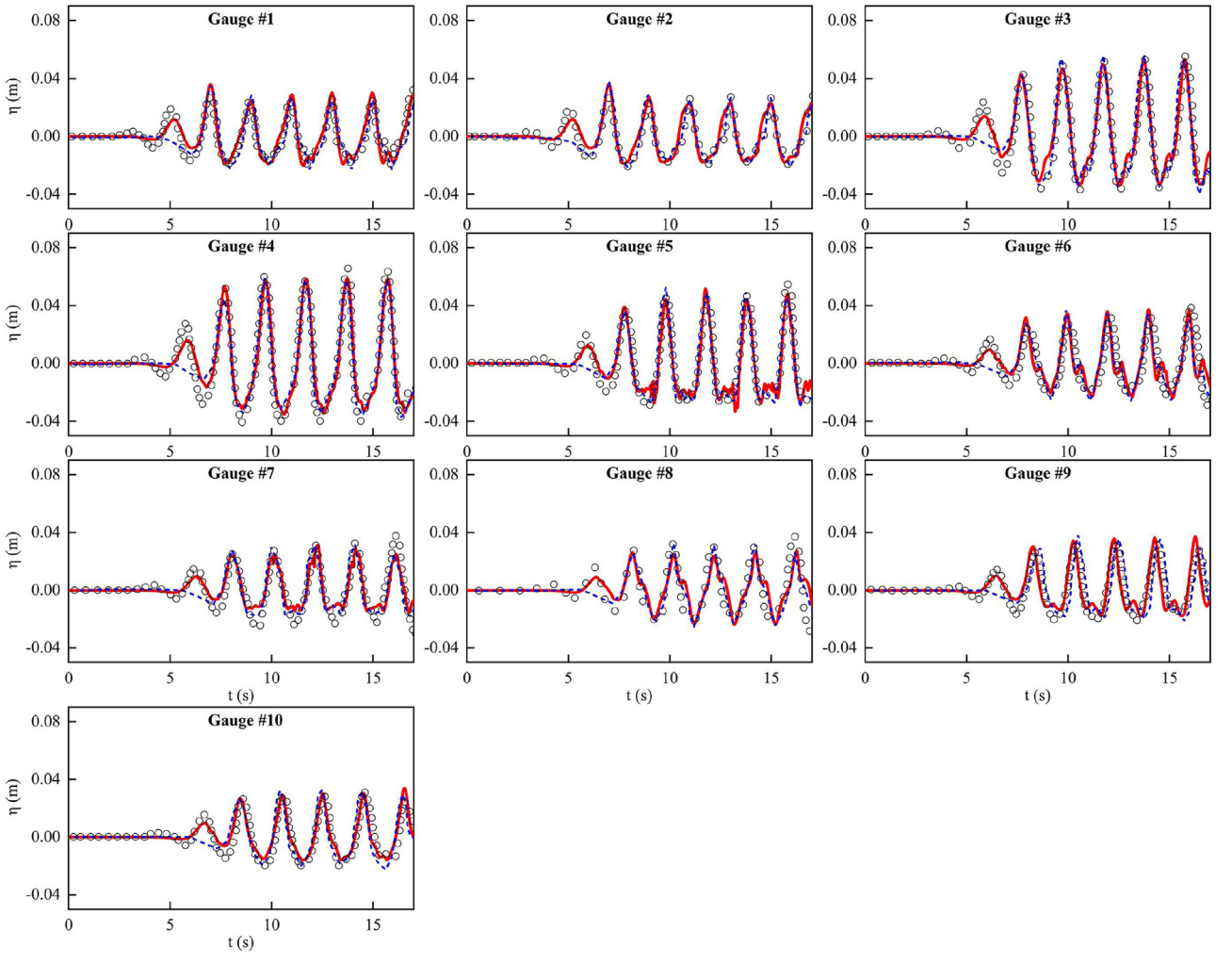

Fig. 15. Comparisons of the numerical results and experimental data for the cnoidal wave case. The red lines represent the numerical results of the proposed model. The blue dashed lines represent the numerical results of the FVM model [50]. The black circles represent the experimental data [50].

Table 7
Comparison of wave crest discrepancy for the LBM model and FVM model.

Gauge number	Δ_{LBM} (%)	Δ_{FVM} (%)	Gauge number	Δ_{LBM} (%)	Δ_{FVM} (%)
WG1	7.93	6.17	WG7	6.73	6.38
WG2	7.54	6.08	WG8	9.38	5.85
WG3	2.05	5.40	WG9	9.16	7.44
WG4	5.36	8.15	WG10	4.73	5.40
WG5	6.74	8.29	Average	6.85	6.87
WG6	8.90	9.51			

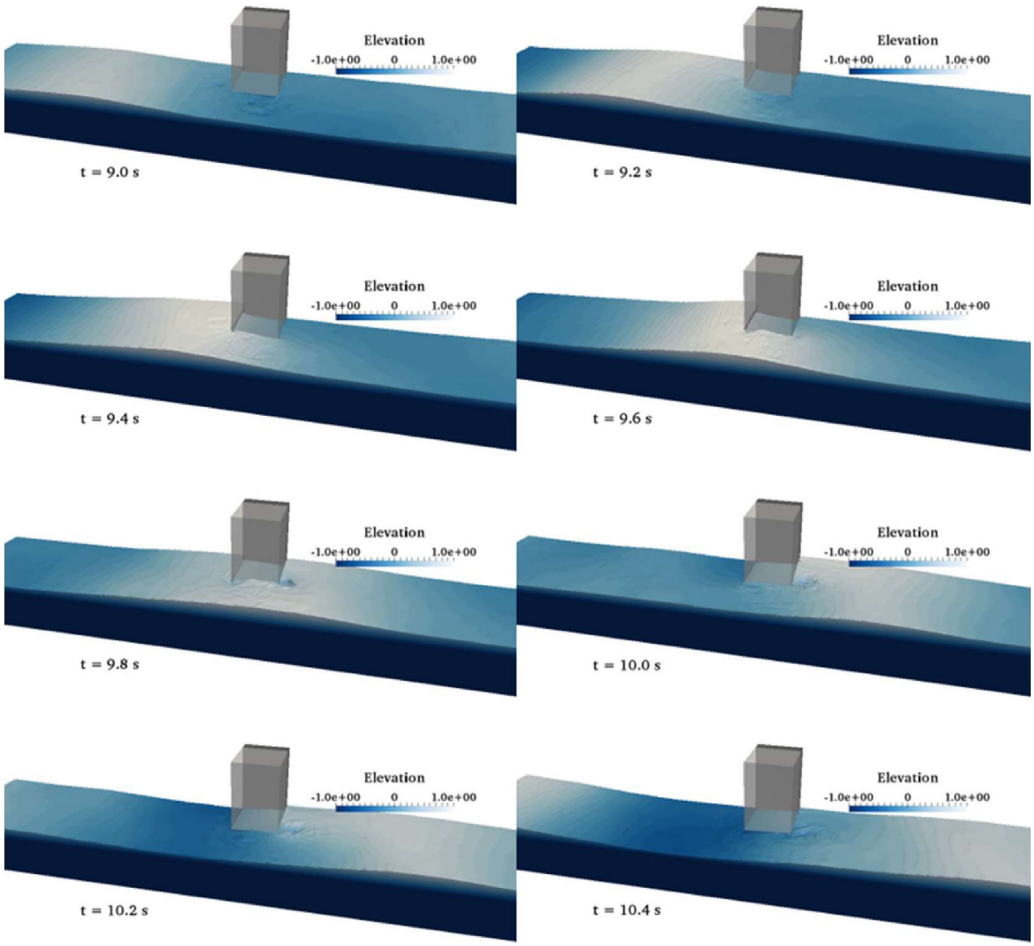

Fig. 16. Cnoidal wave transformation near the permeable vertical breakwater.

18.7% also appear in the FVM simulation results [50]. Several discrepancies occur at the fifth wave crest (gauges 4, 7 and 8) and wave trough (gauges 5, 7 and 9). These aspects are in consonance with the FVM results [50]. Lara et al. [50] highlighted that different reflections at the wave generation boundary may lead to accumulation of discrepancies at the wave crest. Another reason is that the porous media closure cannot completely reproduce the corners of the porous structure at the experiment. Thus, the small ripples generated at the corners have slight difference compared with the experimental data at the wave trough.

Fig. 16 shows some snapshots near the porous structure during a wave period. The phenomena that take place during the cnoidal wave interaction with the porous structure are similar to those of the solitary wave. An elevation delay occurs inside the porous structure due to the resistance force. From $t = 9.2$ s to $t = 9.6$ s, the wave reaches the porous structure, while the free surface elevation inside the porous media is lower than that outside at the same X-plane. From $t = 10.0$ s to $t = 10.2$ s, the wave leaves the porous structure, while the free surface elevation inside the porous medium is slightly higher than that outside at the same X-plane.

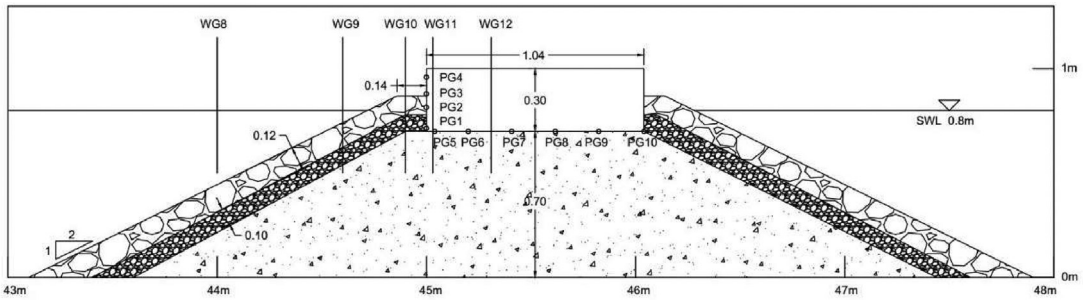

Fig. 17. Sketch of the rubble mound breakwater.

Table 8
Wave gauge positions.

Gauge number	X (m)	Gauge number	X (m)	Gauge number	Z (m)
WG1	17.00	WG5	40.00	WG9	44.60
WG2	37.20	WG6	41.00	WG10	44.90
WG3	38.00	WG7	42.50	WG11	45.03
WG4	38.70	WG8	44.00	WG12	45.31

Table 9
Pressure gauge positions.

Gauge number	X (m)	Y (m)	Gauge number	X (m)	Y (m)
PG1	45.000	0.715	PG6	45.200	0.700
PG2	45.000	0.815	PG7	45.408	0.700
PG3	45.000	0.860	PG8	45.616	0.700
PG4	45.000	0.960	PG9	45.824	0.700
PG5	45.040	0.700	PG10	46.040	0.700

4.3. 3D regular wave interactions with a rubble mound breakwater

4.3.1. Experimental and numerical setups

To evaluate the model's capability in simulating spatially varying porous media, an experiment of regular wave interactions with a rubble mound breakwater [48] is used. The experiment is carried out in a wave flume with a size of 60.0 m $\times$ 2.0 m $\times$ 2.0 m. A sketch of the rubble mound breakwater is shown in Fig. 17. The solid caisson of the breakwater, 1.04 m in length and 0.3 m in height, is placed 45.0 m away from the wave maker, and occupies the whole width of the flume. Below the caisson, the core of the breakwater is made of gravel, 0.7 m in height with a 10 cm berm seaward. The mean diameter and porosity of the core are 0.01 m and 0.49, respectively. A secondary armour layer with a thickness of 10 cm is present on both sides. The mean diameter and porosity of the secondary armour layer are 0.035 m and 0.493, respectively. A 12 cm thick primary armour layer with a 14 cm berm is also laid on both sides. The mean diameter and porosity of the primary armour layer are 0.12 m and 0.5, respectively. The slope of the porous media is 1V/2H. The positions of the wave gauges and pressure gauges are shown in Tables 8 and 9.

To test the performance of our model in the simulation of the 3D wave interactions with the permeable structure, the numerical domain remains in 3D. The numerical wave tank is set up the same as the experiment in length and height but is only 0.1 m in width to reduce the total grid number. Periodic boundary conditions are applied on both side boundaries, while the no-slip boundary conditions are adopted for the other boundaries and solid caisson. The wave condition is the same as that adopted by Higuera et al. [5]. The still water level is 0.8 m; therefore, the structure freeboard is 0.2 m. The wave height and wave period are 20 cm and 3.0 s, respectively. The wave is generated using cnoidal theory. After calibration of the porous friction parameter, the linear parameter is chosen to be 5000 for all porous media. The nonlinear parameters are 2.0, 3.0, and 1.0 for the primary armour layer, secondary armour layer and core, respectively. The LES is used to model the turbulence both inside and outside the porous medium. The Smagorinsky parameter is set to 0.15. Coarse and fine grid sizes of 0.025 and 0.0125 m are adopted in all directions, corresponding to H_{LB} = 8 and 16, respectively, and the Mach number Ma = 0.064. The total grid numbers are 497,280 and 3,978,240, and the total simulation duration is 160 s.

4.3.2. Simulation results

Fig. 18 presents the wave gauge results compared with the experimental data and the former FVM model results [5] at time t = 100-115 s. The first seven gauges are placed in front of the breakwater. The other gauges are placed over the breakwater. Two of them are placed on the top of the caisson to measure violent wave breaking and overtopping.

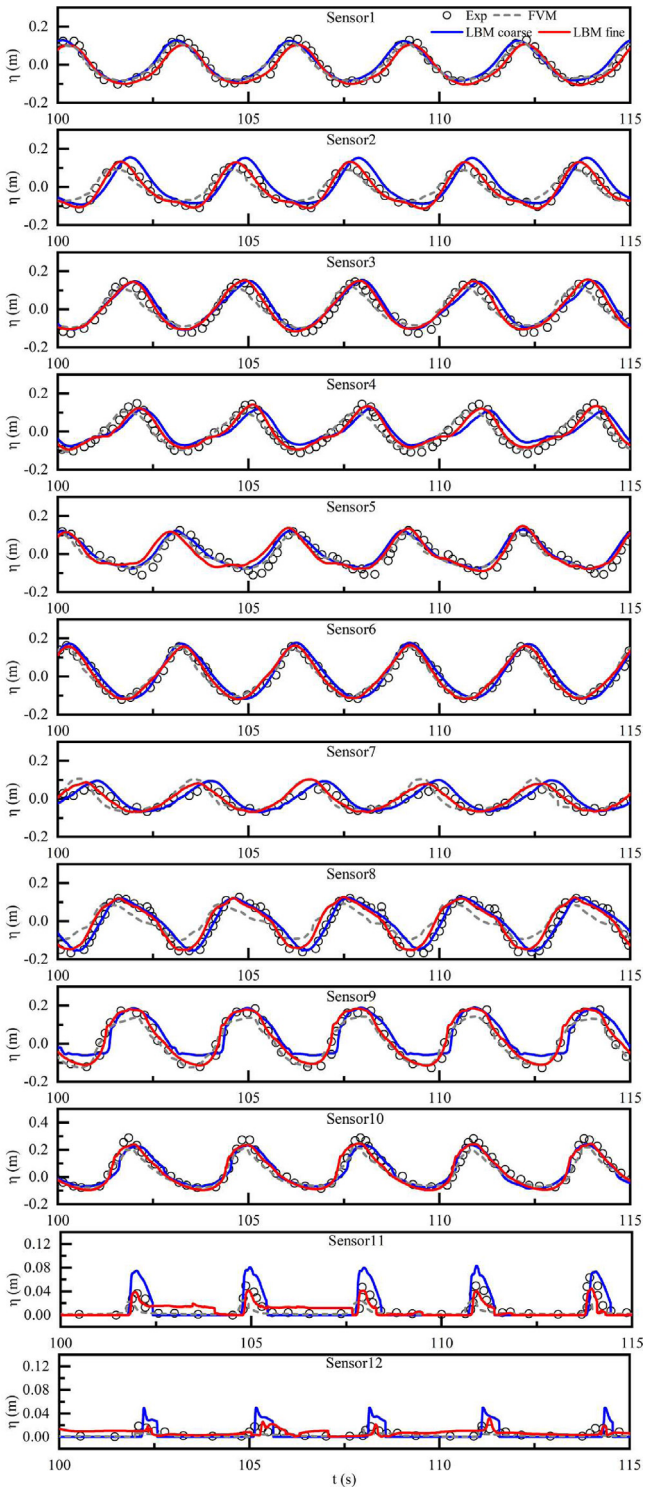

Fig. 18. Comparison of the free surface elevation gauges. The red and blue solid lines represent the numerical results of the proposed model. The grey dashed lines represent the numerical results of the FVM model [5]. The black circles represent the experimental data [5].

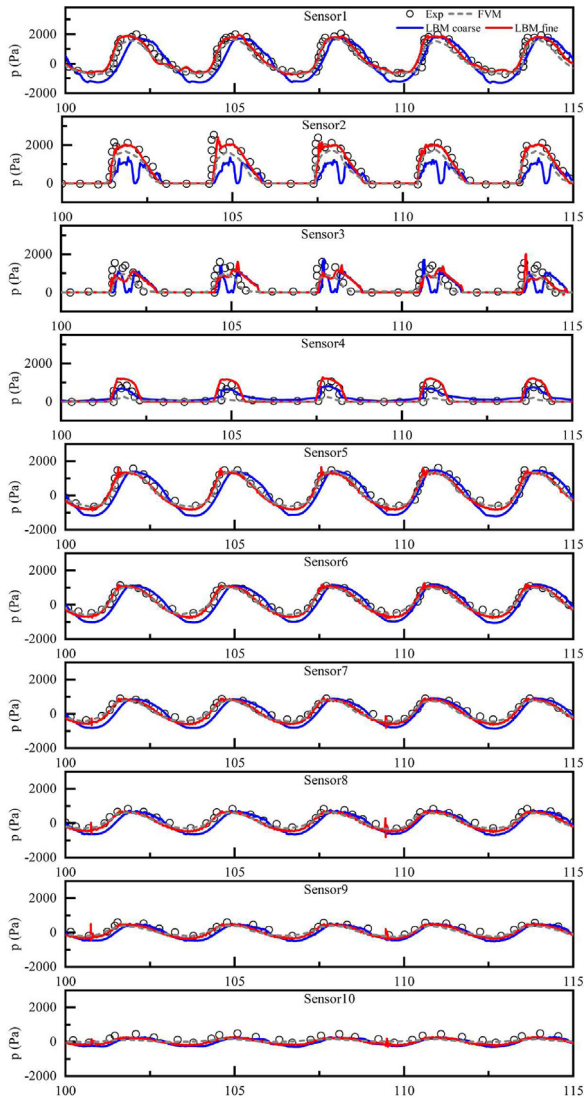

Fig. 19. Comparison of the pressure gauges. The red and blue solid lines represent the numerical results of the proposed model. The grey dashed lines represent the numerical results of the FVM model [5]. The black circles represent the experimental data [5].

For the first seven wave gauges, the coarse and fine grid numerical results of our model show high accuracy compared with that of the experimental data in terms of both the wave heights and phases. These results indicated that the numerical wave tank based on the VANS-LB scheme successfully simulates wave transmission, reflection and percolation due to multi-layer porous media. For the wave gauges above the armour layer (gauges 8-10), the simulation results obtained with fine grids agree with the experimental data. For the wave gauges above the solid caisson (gauges 11 and 12), the simulation results obtained with the fine grids can accurately reflect the crest of overtopping. However, all simulation results exhibit certain discrepancies due to the violent breaking in this area. These discrepancies can be attributed to two aspects. First, as the porous closure is an approximate method, the surface of the porous structure is simplified as a line or a plane. However, in the physical experiment, the primary armour layer is composed of rocks, and the surface is complex with protruding or receding rocks and pores. This aspect can also explain the discrepancy associated with pressure gauges 2 and 3. A similar explanation was presented by Higuera [52]. Second, the VOF free surface method cannot effectively address large deformations. Gauges 11 and 12 are above the solid caisson, where waves break violently and generate many splashing droplets. It is challenging for all models based on the VOF method to describe violent breaking. Above all, all of the free surface gauges show reasonable results and the error is acceptable.

The dynamic pressure results are shown in Fig. 19. The first four pressure gauges are placed seaside of the caisson while the other gauges are set beneath the caisson. Overall, the numerical simulation involving the fine grid accurately predicts the dynamic pressure, particularly the damping effect of the porous media underneath the caisson. Slight oscillation occurs

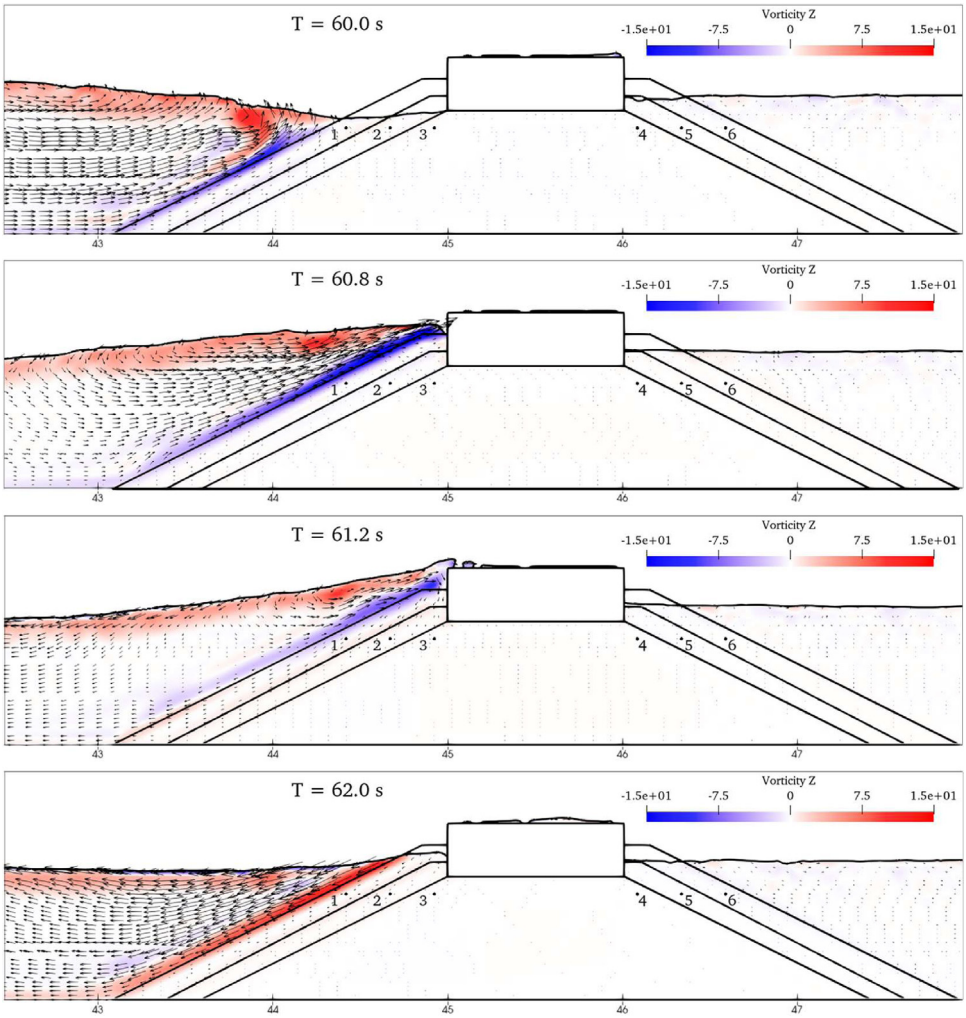

Fig. 20. Velocity vectors and vorticity at slice Z = 0.05 m near the rubble mound breakwater.

Table 10
Velocity gauge positions.

Gauge number	X (m)	Y (m)	Gauge number	X (m)	Y (m)
PG1	44.425	0.6	PG4	46.575	0.6
PG2	44.675	0.6	PG5	46.325	0.6
PG3	44.925	0.6	PG6	46.075	0.6

only at the vertical face of the caisson, especially for pressure gauges 2 and 3. The underestimation of the dynamic pressure is mainly caused by the parametrization of the porous media in a specific area with the same parameters for simplification, which means that the gauges are totally buried in the numerical simulation, while they are partially exposed in the physical experiment. Similar discrepancies also appear in the FVM result.

Fig. 20 shows the velocity vectors and vorticity near the rubble mound breakwater during a wave period. The phenomena of wave run-up, breaking and overtopping near the breakwater are successfully reproduced in our numerical model. Furthermore, the velocity gauge positions at different layers of rubble mound breakwater are shown in Table 10, and the simulation results in the period 50-70 s are shown in Fig. 21. At the up-slope of the breakwater, the velocity gauges exhibit clearly periodicity, and the maximum velocities at different layers are consistent with those reported in the existing research of random wave overtopping of rubble mound breakwater [53]. At the down-slope of the breakwater, the velocities are smaller than those upstream because most of the wave energy is dissipated, and only less of them pass through the permeable breakwater. Due to the impact of the overtopping water, the periodicity is not clear, although a certain periodicity exists.

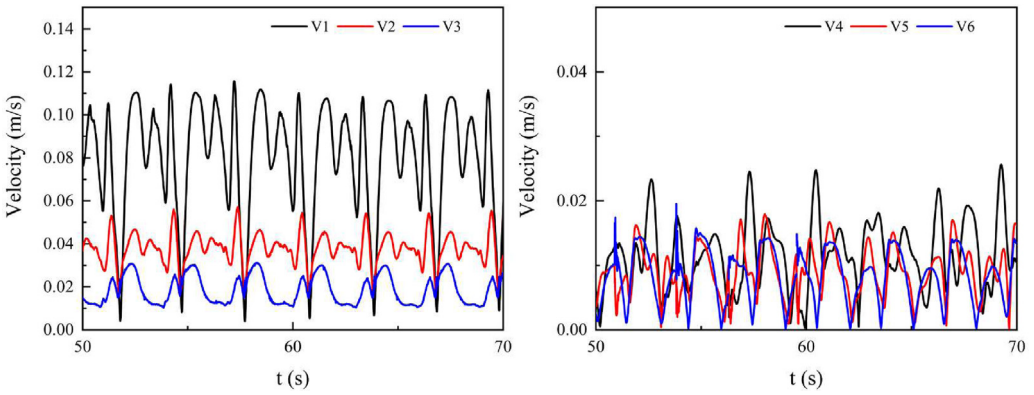

Fig. 21. Velocity gauges at different layers of the rubble mound breakwater.

Table 11
Comparison of the computational efficiency for the calibration of the dam-break case.

Model	f_c (GHz)	N_m (K)	N_c (core)	T_s (s)	T_c (h)	η_{sim} (s·core^{-1}·h^{-1})
IHFoam 2D [5]	2.5	20.6	2	4	0.167	12
WCSPH 2D [8]	3.0	3.3	8	3	0.117	3.21
LBM 2D (present)	3.2	20.6	6	3	1.623×10^{-3}	308.07
IH3VOF 3D [51]	Not mentioned	150	8	4	8	0.063
LBM 3D (present)	3.2	1159	6	3	0.530	0.943

Table 12
Comparison of the computational efficiency for the 3D dam-break case.

Model	f_c (GHz)	N_m (K)	N_c (core)	T_s (s)	T_c (h)	η_{sim} (s·core^{-1}·h^{-1})
IH3VOF [51]	Not mentioned	1135	64	2.5	48	8.138×10^{-4}
WCSPH [12]	2.8	690	30	2.5	60	1.389×10^{-3}
LBM 3D (present)	3.2	1343	6	2.5	0.465	0.896

5. Discussion of the computational efficiency without MPI

As a numerical discretization method, the LBM has a low computational cost and high parallel efficiency due to its local characteristics and non-iterative nature. The computational efficiency, parallel efficiency and scalability of our 3D LBM wave solver on supercomputers with hybrid MPI/OpenMP have already been discussed by Liu et al. [19]. In this section, we discuss the computational efficiency when using a personal PC without MPI.

The numerical simulations described in Sections 3.2 and 4.1 are run on a personal PC with an Intel Core i7-8700 @ 3.20 GHz (6 cores) processor and 2 × DDR4-2400 MHz-8 GB memory. The computational efficiency is defined as

$$\eta_{sim} = \frac{T_s}{T_c N_c} \tag{47}$$

where T_s is the simulation time of the test cases; T_c is the computational cost in real time; N_c is the number of cores used for simulation; f_c is the frequency of the CPU cores; and N_m is the number of mesh or particles. Each case simulated by the LBM is implemented 3 times, and the average computational efficiency is considered. The largest deviation from the average efficiency is less than 2%.

For the calibration dam-break case described in Section 3.2, both 2D and 3D simulations can be performed. To compare the number of meshes and computational efficiency, we present the 2D simulation result using the LBM in Fig. 5. The result is in agreement with the experimental data. A comparison is presented in Table 11. The results show that the computational efficiency η_{sim} of our 2D model is 26 and 96 times that of the IHFoam model and WCSPH model, respectively. The efficiency of our 3D model is 15 times that of the IH3VOF model even though the total grid is nearly 8 times larger than that of the IH3VOF model.

For the 3D dam-break case described in Section 4.1, the comparison is presented in Table 12. The results show that the computational efficiency of the 3D model is 1101 and 645 times those of the IH3VOF model and WCSPH model, respectively.

Although these codes are run on different processors, the large difference of 10 to 1000 times still provides a reference that the proposed model has a high computational efficiency even when the MPI is not used. A similar conclusion was

drawn by Pereira et al. [54], who compared the computational performance of the LBM and SPH in pore scale porous media simulations.

6. Conclusions

This paper proposes a novel three-dimensional multi-relaxation-time Lattice Boltzmann scheme corresponding to the volume-averaged Navier-Stokes equations for studying the interaction of waves and porous structures. Compared with the original LB scheme, the porosity is introduced in the equilibrium distribution function, and the additional friction forces caused by the porous media are added by the discrete force scheme. The single-phase VOF model is established considering the presence of porous media. The turbulence that occurs inside and outside the porous media is calculated using the LES in this model. The following conclusions can be drawn.

(1) The novel VANS-LB scheme can be recovered to the macroscopic governing equations of porous media, Eqs. (1) and (2), by using the Maxwell iteration.
(2) The model parameters pertaining to the porous medium percolation calibrated using the dam-break wave interaction with the porous medium experiment conducted by Lin [44] can be used in other cases.
(3) The simulation results show that the 3D VANS-LB model has an accuracy comparable to that of the FDM, FVM and SPH model. Processes of 3D dam-break wave impacting both solid and porous structures, solitary and cnoidal wave interactions with porous structures, and interaction between regular waves and multi-layer porous structures of rubble mound breakwater can be accurately simulated using the presented LB model.
(4) The discussion of the computational efficiency in this paper and that of the parallel computation with hybrid MPI/OpenMP on a supercomputer presented by Liu et al. [19] together indicate that the LBM model has a higher computational efficiency and parallel scalability compared with those of the other models.

Nevertheless, there remains considerable scope for improvement. Compared with the SPH model, the single-phase VOF in the proposed model is less accurate for large surface deformation phenomena, such as wave breaking. Two-phase flow like phase field model [16] may be used to increase the surface accuracy. Due to the limitations of the cubic lattice and grid uniformity in the adopted conventional LBM model, the total grid number is always larger than that of the FVM model with the advantages of unstructured and polyhedral grids. Local mesh refinement [55] or the cuboid lattice [56] may be incorporated in the proposed model to reduce the total mesh number in future.

Acknowledgement

This study was financially supported by the Joint Funds of the National Natural Science Foundation of China (Grant No. U1906231), Natural Science Foundation of Tianjin (Grant No. 19JCZDJC40200) and National Natural Science Foundation of China (Grant No. 51979190). The simulations were performed on the Tianhe-3 prototype at the National Supercomputer Centre at Tianjin.

References

[1] P.L.F. Liu, P. Lin, K.A. Chang, T. Sakakiyama, Numerical modeling of wave interaction with porous structures, J. Waterw. Port Coast. Ocean Eng 125 (1999) 322–330, doi:10.1061/(ASCE)0733-950X(1999)125:6(322).
[2] T.J. Hsu, T. Sakakiyama, P.L.F. Liu, A numerical model for wave motions and turbulence flows in front of a composite breakwater, Coast. Eng. 46 (2002) 25–50, doi:10.1016/S0378-3839(02)00045-5.
[3] K.C. Hu, S.C. Hsiao, H.H. Hwung, T.R. Wu, Three-dimensional numerical modeling of the interaction of dam-break waves and porous media, Adv. Water Resour. 47 (2012) 14–30, doi:10.1016/j.advwatres.2012.06.007.
[4] M. del Jesus, J.L. Lara, I.J. Losada, Three-dimensional interaction of waves and porous coastal structures Part I: numerical model formulation, Coast. Eng. 64 (2012) 57–72, doi:10.1016/j.coastaleng.2012.01.008.
[5] P. Higuera, J.L. Lara, I.J. Losada, Three-dimensional interaction of waves and porous coastal structures using OpenFOAM®. Part I: formulation and validation, Coast. Eng. 83 (2014) 243–258, doi:10.1016/j.coastaleng.2013.08.010.
[6] S. Shao, Incompressible SPH flow model for wave interactions with porous media, Coast. Eng. 57 (2010) 304–316, doi:10.1016/j.coastaleng.2009.10.012.
[7] B. Ren, H. Wen, P. Dong, Y. Wang, Numerical simulation of wave interaction with porous structures using an improved smoothed particle hydrodynamic method, Coast. Eng. 88 (2014) 88–100, doi:10.1016/j.coastaleng.2014.02.006.
[8] B. Ren, H. Wen, P. Dong, Y. Wang, Improved SPH simulation of wave motions and turbulent flows through porous media, Coast. Eng. 107 (2016) 14–27, doi:10.1016/j.coastaleng.2015.10.004.
[9] A. Khayyer, H. Gotoh, Y. Shimizu, K. Gotoh, H. Falahaty, S. Shao, Development of a projection-based SPH method for numerical wave flume with porous media of variable porosity, Coast. Eng. 140 (2018) 1–22, doi:10.1016/j.coastaleng.2018.05.003.
[10] R. Divya, V. Sriram, Wave-porous structure interaction modelling using Improved Meshless Local Petrov Galerkin method, Appl. Ocean Res. 67 (2017) 291–305, doi:10.1016/j.apor.2017.07.017.
[11] R. Divya, V. Sriram, K. Murali, Wave-vegetation interaction using Improved Meshless Local Petrov Galerkin method, Appl. Ocean Res. 101 (2020), doi:10.1016/j.apor.2020.102116.
[12] H. Wen, B. Ren, G. Wang, 3D SPH porous flow model for wave interaction with permeable structures, Appl. Ocean Res. 75 (2018) 223–233, doi:10.1016/j.apor.2018.04.003.
[13] C.F. Janßen, S.T. Grilli, M. Krafczyk, On enhanced non-linear free surface flow simulations with a hybrid LBM–VOF model, Comput. Math. Appl. 65 (2013) 211–229, doi:10.1016/j.camwa.2012.05.012.
[14] Y. Thorimbert, J. Latt, L. Cappietti, B. Chopard, Virtual wave flume and Oscillating Water Column modeled by lattice Boltzmann method and comparison with experimental data, Int. J. Mar. Energy 14 (2016) 41–51, doi:10.1016/j.ijome.2016.04.001.
[15] A. Badarch, J.D. Fenton, T. Hosoyamada, Application of free-surface immersed-boundary lattice Boltzmann method to waves acting on coastal structures, J. Hydraul. Eng. (2020) 146, doi:10.1061/(asce)hy.1943-7900.0001679.

[16] D.E. Kumar, S.A. Sannasiraj, V. Sundar, Phase field lattice Boltzmann model for air-water two phase flows, Phys. Fluids 31 (2019), doi:10.1063/1.5100215.
[17] G. Liu, Q. Zhang, J. Zhang, Numerical wave simulation using a modified lattice Boltzmann scheme, Comput. Fluids 184 (2019) 153–164, doi:10.1016/j.compfluid.2019.03.005.
[18] G.-w. Liu, Q.-h. Zhang, J.-f. Zhang, Development of two-dimensional numerical wave tank based on lattice Boltzmann method, J. Hydrodyn. 32 (2020) 116–125, doi:10.1007/s42241-019-0039-8.
[19] G. Liu, J. Zhang, Q. Zhang, A high-performance three-dimensional lattice Boltzmann solver for water waves with free surface capturing, Coast. Eng. 165 (2021), doi:10.1016/j.coastaleng.2021.103865.
[20] S.D.C. Walsh, H. Burwinkle, M.O. Saar, A new partial-bounceback lattice-Boltzmann method for fluid flow through heterogeneous media, Comput. Geosci. 35 (2009) 1186–1193, doi:10.1016/j.cageo.2008.05.004.
[21] B.D. Wood, X. He, S.V. Apte, Modeling turbulent flows in porous media, Annu. Rev. Fluid Mech. 52 (2020) 171–203, doi:10.1146/annurev-fluid-010719-060317.
[22] S. Succi, E. Foti, F. Higuera, Three-dimensional flows in complex geometries with the lattice boltzmann method, Europhys. Lett. 10 (1989) 433–438, doi:10.1209/0295-5075/10/5/008.
[23] Y.F. Liu, D.S. Jeng, Pore scale study of the influence of particle geometry on soil permeability, Adv. Water Resour. 129 (2019) 232–249, doi:10.1016/j.advwatres.2019.05.024.
[24] X. Zhang, L.-l. Wang, H. Zhu, C. Zeng, Pore-scale simulation of salt fingers in porous media using a coupled iterative source-correction immersed boundary-lattice Boltzmann solver, Appl. Math. Modell. 94 (2021) 656–675, doi:10.1016/j.apm.2021.01.019.
[25] G.G. Pereira, A multiphase single relaxation time lattice Boltzmann model for heterogeneous porous media, Appl. Math. Modell. 44 (2017) 160–174, doi:10.1016/j.apm.2016.11.009.
[26] G.G. Pereira, Fluid flow, relative permeabilities and capillary pressure curves through heterogeneous porous media, Appl. Math. Modell. 75 (2019) 481–493, doi:10.1016/j.apm.2019.05.050.
[27] K. Suga, Y. Kuwata, K. Takashima, R. Chikasue, A D3Q27 multiple-relaxation-time lattice Boltzmann method for turbulent flows, Comput. Math. Appl. 69 (2015) 518–529, doi:10.1016/j.camwa.2015.01.010.
[28] Z. Guo, T.S. Zhao, Lattice Boltzmann model for incompressible flows through porous media, Phys. Rev. E 66 (2002), doi:10.1103/PhysRevE.66.036304.
[29] J. Zhang, L. Wang, J. Ouyang, Lattice Boltzmann model for the volume-averaged Navier-Stokes equations, Europhys. Lett. 107 (2014), doi:10.1209/0295-5075/107/20001.
[30] B. Blais, J.-M. Tucny, D. Vidal, F. Bertrand, A conservative lattice Boltzmann model for the volume-averaged Navier–Stokes equations based on a novel collision operator, J. Comput. Phys. 294 (2015) 258–273, doi:10.1016/j.jcp.2015.03.036.
[31] S.B. Höcker, R. Trunk, W. Dörfler, M.J. Krause, Towards the simulations of inertial dense particulate flows with a volume-averaged lattice Boltzmann method, Comput. Fluids 166 (2018) 152–162, doi:10.1016/j.compfluid.2018.02.011.
[32] T. Maruyama, Large eddy simulation of turbulent flow around a windbreak, J. Wind Eng. Ind. Aerodyn. 96 (2008) 1998–2006, doi:10.1016/j.jweia.2008.02.062.
[33] P.Y. Polubarinova-Kochina, Theory of Ground Water Movement, Princeton University, 1962.
[34] F. Engelund, in: On the Laminar and Turbulent Flows of Ground Water through Homogeneous Sand, Transactions of the Danish: Academy of Technical Sciences, 1953, pp. 356–361.
[35] M. van Gent, Wave Interaction with Permeable Coastal Structures Ph.D. Thesis, Delft University of Technology, 1995.
[36] D. D'Humières, I. Ginzburg, M. Krafczyk, P. Lallemand, L.S. Luo, Multiple-relaxation-time lattice Boltzmann models in three dimensions, Phil. Trans. R. Soc. A 360 (2002) 437–451, doi:10.1098/rsta.2001.0955.
[37] Z. Guo, C. Zheng, B. Shi, Discrete lattice effects on the forcing term in the lattice Boltzmann method, Phys. Rev. E 65 (2002) 046308, doi:10.1103/PhysRevE.65.046308.
[38] M. Krafczyk, J. Tölke, L.S. Luo, Large-eddy simulations with a multiple-relaxation-time LBE model, Int. J. Mod. Phys. B 17 (2003) 33–39, doi:10.1142/s0217979203017059.
[39] W.A. Yong, W. Zhao, L.S. Luo, Theory of the Lattice Boltzmann method: derivation of macroscopic equations via the Maxwell iteration, Phys. Rev. E 93 (2016) 033310, doi:10.1103/PhysRevE.93.033310.
[40] Z. Guo, C. Zheng, B. Shi, An extrapolation method for boundary conditions in lattice Boltzmann method, Phys. Fluids 14 (2002) 2007–2010, doi:10.1063/1.1471914.
[41] P. Higuera, J.L. Lara, I.J. Losada, Realistic wave generation and active wave absorption for Navier–Stokes models, Coast. Eng. 71 (2013) 102–118, doi:10.1016/j.coastaleng.2012.07.002.
[42] N. Thürey, A Lattice Boltzmann Method for Single-Phase Free Surface Flows in 3D Master Thesis, Erlangen University, 2003.
[43] C. Körner, M. Thies, T. Hofmann, N. Thürey, U. Rüde, Lattice Boltzmann model for free surface flow for modeling foaming, J. Stat. Phys. 121 (2005) 179–196, doi:10.1007/s10955-005-8879-8.
[44] P. Lin, Numerical Modeling of Breaking Waves PH.D. Thesis, Cornell University, 1998.
[45] I.J. Losada, J.L. Lara, M. del Jesus, Modeling the interaction of water waves with porous coastal structures, J. Waterw. Port Coastal Ocean Eng. 142 (2016), doi:10.1061/(asce)ww.1943-5460.0000361.
[46] H.F. Burcharth, O.K. Andersen, On the one-dimensional steady and unsteady porous flow equations, Coast. Eng. 24 (1995) 233–257, doi:10.1016/0378-3839(94)00025-S.
[47] X. He, L.S. Luo, Lattice Boltzmann model for the incompressible Navier-Stokes equation, J. Stat. Phys. 88 (1997) 927–944, doi:10.1023/b:joss.0000015179.12689.e4.
[48] I.J. Losada, J.L. Lara, R. Guanche, J.M. Gonzalez-Ondina, Numerical analysis of wave overtopping of rubble mound breakwaters, Coast. Eng. 55 (2008) 47–62, doi:10.1016/j.coastaleng.2007.06.003.
[49] T.-R. Wu, A numerical study of three-dimensional breaking waves and turbulence effects PH.D. Thesis, Cornell University, 2004.
[50] J.L. Lara, M. del Jesus, I.J. Losada, Three-dimensional interaction of waves and porous coastal structures Part II: experimental validation, Coast. Eng. 64 (2012) 26–46, doi:10.1016/j.coastaleng.2012.01.009.
[51] M. del Jesus, Three-Dimensional Interaction of Water Waves with Maritime Structures PH.D. Thesis, University of Cantabria, 2011.
[52] P. Higuera, Application of Computational Fluid Dynamics to Wave Action on Structures Ph.D. Thesis, Universidade de Cantabria, 2015.
[53] J.-y. Li, Q.-h. Zhang, Y.-j. Lu, Numerical simulation of random wave overtopping of rubble mound breakwater with armor units, China Ocean Eng. 35 (2021) 176–185, doi:10.1007/s13344-021-0016-1.
[54] G.G. Pereira, P.M. Dupuy, P.W. Cleary, G.W. Delaney, Comparison of permeability of model porous media between SPH and LB, Prog. Comput. Fluid Dyn. 12 (2012) 176–186, doi:10.1504/PCFD.2012.047460.
[55] D. Lagrava, O. Malaspinas, J. Latt, B. Chopard, Advances in multi-domain lattice Boltzmann grid refinement, J. Comput. Phys. 231 (2012) 4808–4822, doi:10.1016/j.jcp.2012.03.015.
[56] E. Yahia, W. Schupbach, K. Premnath, Three-dimensional central moment lattice Boltzmann method on a cuboid lattice for anisotropic and inhomogeneous flows, Fluids 6 (2021) 326, doi:10.3390/fluids6090326.